EZH1-dependent H3K27me1 is an adaptive chromatin barrier that limits DNMT inhibitor response in colorectal cancer

Alison A. Chomiak[1,*], Ashley K. Wiseman[1,*], Joel A. Hrit[1], Yanqing Liu[1,2], Stephanie Stransky[3], Ying Cui[4], Xiangqian Kong[4], Michael J. Topper[4], Stephen B. Baylin[4], Simone Sidoli[3], Rochelle L. Tiedemann[1], and Scott B. Rothbart[1,2,†]

[1] Department of Epigenetics, Van Andel Institute, Grand Rapids, Michigan 49503, USA.

[2] Van Andel Institute Graduate School, Grand Rapids, Michigan 49503, USA.

[3] Department of Biochemistry, Albert Einstein College of Medicine, Bronx, New York 10461, USA.

[4] The Sidney Kimmel Comprehensive Cancer Center at Johns Hopkins, The Johns Hopkins University School of Medicine, Baltimore, MD, 21287, USA.

*first authors

[†]Correspondence: scott.rothbart@vai.org, 616-234-5367

Keywords

DNA methylation, histone PTMs, PRC2, EZH1, EZH2, H3K27me1, colorectal cancer, epigenetic plasticity

Highlights

- EZH1-dependent H3K27me1 sustains an adaptive barrier to DNMT inhibitor response in colorectal cancer.
- Dual EZH1/2 inhibition eliminates all H3K27 methylation states and remodels chromatin architecture.
- EZH inhibition induces a DNA methylation-H3K27ac bivalent chromatin state.
- DNMT and EZH1/2 co-inhibition reprograms enhancers and promoters to activate tumor-suppressive pathways.
- Combination therapy suppresses MYC/E2F-driven oncogenic transcription, defining its cancer cell-intrinsic therapeutic efficacy.

Abstract

Abnormal DNA methylation patterning is a defining epigenetic hallmark of human cancer and is therapeutically targetable with DNA methyltransferase inhibitors (DNMTi's). However, DNMTi-induced DNA hypomethylation promotes adaptive chromatin remodeling that limits molecular and therapeutic responses to these drugs. Here, we identify EZH1-dependent H3K27 mono-methylation (H3K27me1) as a previously unrecognized adaptive barrier to DNMTi response in colorectal cancer. While EZH2-selective inhibitors deplete H3K27me2 and H3K27me3, they preserve EZH1-dependent H3K27me1 at Polycomb-enriched genomic regions. In contrast, dual EZH1/2 inhibition eliminates all H3K27 methylation states and robustly synergizes with DNMTi to enhance transcriptional activation and growth suppression. Mechanistically, dual EZH1/2 inhibition induces a redistribution of p300/CBP-dependent H3K27 acetylation (H3K27ac), generating a therapy-associated bivalent chromatin state characterized by coexisting DNA methylation and H3K27ac. DNMT inhibition resolves this induced bivalency, enabling activation of tumor-suppressive transcriptional programs. At the same time, coordinated loss of H3K27me1 and gene-body DNA methylation, together with depletion of promoter-associated H3K27ac, suppresses MYC- and E2F-driven oncogenic transcription networks that define the cancer cell-intrinsic therapeutic response. Collectively, these findings establish EZH1-dependent H3K27me1 as a key mediator of adaptive epigenetic plasticity and provide mechanistic rationale for combining DNMT inhibitors with dual EZH1/2i inhibitors to reprogram chromatin and suppress oncogenic transcription in solid tumors.

Introduction

Abnormal DNA methylation patterning and dysregulated histone post-translational modification (PTM) signaling are defining epigenetic hallmarks of human cancer that drive tumor initiation and progression through their effects on transcriptional reprogramming (1,2). Unlike genetic mutations, epigenetic alterations are reversible through targeting the enzymes that write, erase, and read these marks (3). The most clinically advanced class of drugs targeting epigenetic regulators are nucleoside analog DNA methyltransferase inhibitors like azacitidine (vidaza; AZA) and 5-aza-2'-deoxycytidine (decitabine; DAC) that can restore expression of silenced tumor suppressor genes (TSG's) and transposable elements (TE's) that stimulate innate immune signaling through the induction of viral mimicry (4,5). While these drugs have found clinical success with U.S. Food and Drug Administration (FDA) approvals for hematological malignancies (6–8), their efficacy in solid tumors has remained limited due to their short half-life in circulation and dose-limiting toxicities at concentrations needed to reach exposure levels that mirror effects in preclinical models (9,10).

In addition to these pharmacologic constraints, our group and others have shown that DNMTi-induced DNA hypomethylation induces adaptive epigenetic reprogramming. This reprogramming counteracts transcriptional reactivation by reinforcing TSG and innate immune pathway silencing through compensatory acquisition of repressive histone PTMs (11–14). Prominent among these adaptive responses is increased activity of EZH2, the major catalytic subunit of Polycomb Repressive Complex 2 (PRC2). PRC2 is responsible for the deposition of lysine 27 tri-methylation on histone H3 (H3K27me3), a defining histone PTM signature of facultative heterochromatin. In our prior work, we showed that inhibition of EZH2-dependent H3K27me3 synergizes with DNMTi to enhance viral mimicry and anti-tumor responses (11,12), establishing PRC2 as a central mediator of DNMTi-induced epigenetic plasticity.

In response to the identification of EZH2 as a therapeutic vulnerability in several tumor types (15,16), recent drug discovery efforts have yielded a growing arsenal of inhibitors targeting EZH2 and other core and accessory subunits of PRC2. The most clinically advanced of these agents is tazemetostat (TAZ; EPZ-6438), an EZH2 inhibitor (EZH2i) with FDA approvals for epithelioid sarcoma and follicular lymphoma (17,18), and several additional compounds are advancing through clinical trials. However,

despite this progress, PRC2-directed inhibitors have not been systematically compared or evaluated in combination with DNMTi. This gap presents a timely opportunity to define which PRC2-directed strategies are best suited to overcome DNMTi-induced adaptive chromatin responses.

Here, we show that while EZH2-selective inhibitors, including TAZ, synergize with DNMTi, dual inhibition of EZH1 and EZH2, paralogous and interchangeable catalytic subunits of PRC2, is markedly more effective in colorectal cancer (CRC). We identify EZH1-mediated lysine 27 mono-methylation on histone H3 (H3K27me1) as a previously unrecognized adaptive barrier to DNMTi response in CRC. Dual EZH1/2 inhibition eliminates all three H3K27 states, driving redistribution of p300/CBP-dependent H3K27 acetylation (H3K27ac). When combined with DNMTi, this resolves a therapy-induced bivalent chromatin state to simultaneously stimulate tumor-suppressive transcriptional programs and constrain oncogenic transcription. Together, these findings establish EZH1-dependent H3K27me1 as a key mediator of DNMTi-induced chromatin plasticity and define dual EZH1/2 inhibition as a mechanistically grounded strategy to enhance DNMTi therapeutic efficacy in solid tumors.

Results

Dual EZH1/2 inhibition distinguishes PRC2 inhibitors that potentiate DNMTi-induced transcription

Our prior studies showed that the clinically relevant EZH2i TAZ enhances DNMTi-induced transcriptional activation in CRC cells (11). Building on this work, we sought to determine whether additional pharmacologic strategies targeting PRC2 could further potentiate DNMTi-mediated de-repression of DNA methylation-regulated genes. To facilitate this, we leveraged our previously described *SFRP1*-Nanoluciferase (NLuc) transcriptional reporter line engineered in the HCT116 colon cancer cell line (11). In this reporter line, promoter CpG island hypermethylation silences an endogenous allele of the TSG *SFRP1*, and insertion of NLuc into exon 2 of this locus provides a quantitative readout of *SFRP1* re-expression from its native chromatin context. Importantly, this reporter line was engineered in a *DNMT1* hypomorphic background with 20% global DNA methylation reduction compared to parental cells (19), thereby sensitizing the system to detect additive or synergistic chromatin de-repression events.

Using the *SFRP1*-NLuc reporter line, we screened a diverse panel of PRC2-directed chemical probes, including experimental and clinically applied SAM-competitive inhibitors of EZH2 and EZH1, protein-protein interaction (PPI) disruptors targeting EED, and PROTAC degraders of PRC2 subunits (**Figure 1A-B** and **S1A-B**). Among these compounds, three SAM-competitive inhibitors – tulmimetostat (CPI-0209; TUL) (20,21), valemetostat (DS3201b; VAL) (22–24), and mevrometostat (PF-1497; MEV) (25,26) – were most effective at inducing re-expression of *SFRP1* when combined with a low dose of the DNMTi DAC (30 nM) that mirrors clinically relevant *in vivo* exposure (11). Consistent with our previous findings (11), PRC2 inhibitors that most robustly induced transcription exhibited minimal toxicity as single agents (**Figure S1C-D**), suggesting that several of these other compounds have off-target toxicities. Notably, VAL, TUL, and MEV (the three top-performing inhibitors in this screen) are also among the most clinically advanced PRC2 inhibitors (21,23–25,27), suggesting that they share a therapeutically relevant mode of action.

To define the mechanistic features distinguishing these compounds from less efficacious PRC2 inhibitors, we analyzed global H3K27 methylation states by western blotting. PRC2 catalyzes all three methylation states of H3K27 (H3K27me1/me2/me3), and the most effective compounds (TUL, VAL, and MEV) reduced all three methylation states on H3K27 (**Figure 1C** and **S1E-F**). Notably, loss of H3K27me1 was unique to the most efficacious compounds, whereas selective loss of H3K27me3, the most commonly studied PRC2 product, did not correlate with transcriptional activation potential.

Previous studies have shown that EZH1-containing PRC2 complexes preferentially catalyze H3K27 mono-methylation and are enriched at chromatin regions marked by H3K27me1 (28–31). Together with reports that both VAL and TUL inhibit EZH1 in addition to EZH2 (20,22), these observations led us to hypothesize that dual EZH1 and EZH2 inhibition underlies the superior transcriptional activation potential of these compounds. To test this directly, we measured the inhibitory activity of six representative PRC2 antagonists towards recombinant EZH1- and EZH2-containing PRC2 core complexes using *in vitro* methyltransferase activity assays with recombinant nucleosome substrates (**Figure 1D**). Indeed, TUL, VAL, and MEV potently inhibited both EZH1- and EZH2-containing PRC2 complex activity in a dose-dependent manner (**Figure 1D**). In contrast, TAZ (consistent with its

intermediate efficacy in the NLuc reporter assay (**Figure 1A-B**)) preferentially inhibited EZH2-containing PRC2 complexes (**Figure 1D**). GSK126 and UNC1999, which performed poorly in the NLuc reporter assay (**Figure 1A**), were weak inhibitors of both EZH1- and EZH2-containing PRC2 complexes (**Figure 1D**). Comparison of IC_{50} values showed that the most effective compounds inhibited both EZH1- and EZH2-containing PRC2 complexes at low nanomolar concentrations, whereas less efficacious compounds preferentially targeted EZH2 or inhibited both complexes only at micromolar concentrations (**Figure 1E**).

Collectively, these results demonstrate that dual inhibition of EZH1 and EZH2, accompanied by ablation of all three H3K27 methylation states, are distinguishing characteristics of PRC2 inhibitors that are most effective at enhancing the transcriptional activating effects of DNMTi.

EZH1 expression stratifies clinical outcome and cellular sensitivity to dual EZH1/2 inhibition

While the role of EZH2 and H3K27me3 in cancer has been extensively studied (32), the contribution of EZH1 to H3K27 methylation states in cancer, and the molecular mechanism underlying this efficacy, is less clear (33,34). Prior *in vitro* biochemical studies, genetic knockout experiments in mouse embryonic stem cells (mESCs), and differentiation studies in mESCs have implicated EZH1 in maintaining H3K27me1, particularly in contexts where EZH2 is reduced or absent (29–31,35). Based on these observations, we hypothesized that EZH1 maintains H3K27me1 to preserve a repressive chromatin environment when EZH2 activity is lost or inhibited in colon cancer cells, and that EZH1 expression levels may therefore be predictive of responsiveness to EZH2-selective versus dual EZH1/2 inhibitors.

To assess the clinical relevance of EZH1 in colon cancer, we first examined the association between EZH1 expression and patient outcomes in TCGA COADREAD (colon adenocarcinoma/rectal adenocarcinoma) tumors. EZH1 mRNA expression, but not EZH2, stratified patient survival in this cohort (**Figure 2A** and **S2A**), suggesting a unique role for EZH1 in disease progression.

We next asked whether elevated EZH1 expression confers a functional vulnerability to PRC2 inhibition. From a panel of CRC cell lines with variable EZH1 expression levels (**Figure 2B**), we selected

RKO cells with high EZH1 expression, HCT116 cells with intermediate EZH1 expression, and SW620 with low EZH1 expression. Cells were treated with either the EZH2-selective inhibitor TAZ or the dual EZH1/2 inhibitor VAL at doses that comparably reduced H3K27me3 levels within each cell line (**Figure S1F** and **S2B**) in combination with DAC at a concentration that produced moderate effects on cell proliferation (**Figure 2C**). Notably, RKO cells exhibited significantly greater sensitivity to VAL in combination with DAC compared to TAZ, whereas HCT116 and SW620 displayed progressively diminished differential responses (**Figure 2C**).

Together, these data indicate that EZH1 expression is associated with survival in CRC and predicts enhanced cellular sensitivity to dual EZH1/2 inhibition. These findings support EZH1 as a mechanistic contributor to PRC2-mediated adaptive repression to DNMTi therapy and identify EZH1 as a potential biomarker for stratifying clinical responses to PRC2-directed combination therapy.

EZH1 contributes to H3K27 mono-methylation maintenance when EZH2 is inhibited

To define the mechanistic contribution of EZH1 to PRC2-dependent chromatin regulation in CRC, we generated isogenic EZH1- and EZH2-knockout (KO) RKO cell lines, alongside control-KO lines targeting a gene desert on chromosome 12, using CRISPR/Cas9. RKO cells were chosen due to their high endogenous expression levels of both EZH1 and EZH2 (**Figure 2B**). Successful gene disruption in clonally expanded cell populations was confirmed by western blot analyses and genomic sequencing (**Figure 3A** and **S3A**). Western blot analysis of all three H3K27 methylation states in these KO lines, with or without DAC treatment, revealed that while EZH1-KO had no effect on global H3K27 methylation levels, EZH2-KO showed reduced global levels of H3K27me2 and H3K27me3, accompanied by a marked increase in H3K27me1 levels relative to control-KO lines (**Figure 3B**).

To validate these findings in an antibody-independent manner, and to comprehensively assess histone PTM remodeling, we performed quantitative histone PTM mass spectrometry on these KO lines. Consistent with western blot analyses, EZH1-KO cells showed minimal changes in the distribution of H3K27 methylation states compared to control-KO cells (**Figure 3C**). In contrast, EZH2-KO cells showed pronounced reductions in H3K27me2 and H3K27me3 on both canonical H3.1 and variant H3.3, coupled

with increased H3K27me1 on H3.1 and maintenance of H3K27me1 on H3.3 (**Figure 3C**). As expected from the reported antagonistic relationship between H3K27 and H3K36 methylation (36,37), EZH2 loss was also associated with increased H3K36 methylation, along with several additional minor PTM changes compared to both control-KO and EZH1-KO clones (**Figure S3B**).

To directly test whether EZH1 is responsible for the compensatory increase in H3K27me1 observed upon EZH2 loss, and to circumvent the lethality of dual EZH1- and EZH2-KO in these cells, we introduced a doxycycline-inducible shRNA targeting EZH1 into an EZH2-KO clone background. Indeed, shRNA-mediated EZH1 knockdown (KD) in EZH2-KO cells mitigated the EZH2-KO-associated increase in H3K27me1, assessed by both western blotting and histone PTM mass spectrometry (**Figure 3D-E)**. Additional gains of H3K36 methylation followed dual depletion compared to EZH2-KO alone (**Figure S3C).** Notably, both EZH2-KO cells and EZH1 and EZH2 dually depleted cells showed increased acetylation at H3K27 (H3K27ac), but not at H3K18 (H3K18ac) (**Figure 3F**). Given that both residues are substrates for p300/CBP histone acetyltransferase activity, these data indicate selective remodeling of H3K27ac following dual EZH1/2 loss.

We next asked whether pharmacologic inhibition of EZH1 and EZH2 recapitulates these genetic phenotypes. Consistent with EZH2 genetic ablation, treatment of RKO cells with the EZH2-selective inhibitor TAZ, alone or in combination with DAC, reduced H3K27me2 and H3K27me3 while increasing H3K27me1 (**Figure 3G** and **S3D-E**). In contrast, treatment with the dual EZH1/2 inhibitor VAL, alone or in combination with DAC, resulted in loss of all three H3K27 methylation states, phenocopying results of combined EZH1-KD and EZH2-KO (**Figure 3G** and **S3D-E**). Similar to genetic perturbation, both TAZ and VAL increased H3K27ac levels without affecting H3K18ac or other histone acetylation sites (**Figure 3H** and **S3F**).

Collectively, these data show that EZH1 maintains H3K27me1 in the setting of EZH2 loss or inhibition, and that ablation of this EZH1-dependent activity distinguishes dual EZH1/2 inhibitors from EZH2-selective compounds. Importantly, these findings begin to reveal a mechanistic basis for the enhanced efficacy of dual EZH1/2 inhibition and establish EZH1-dependent H3K27me1 as a critical adaptive chromatin barrier in CRC.

Context-dependent genomic redistribution of H3K27me1 reveals distinct EZH1 and EZH2 functions

To define the genomic locations where EZH1/2 inhibitor-induced H3K27me1 dynamics were observable, we next analyzed genome-wide H3K27me1 distributions in drug-treated RKO cells. To enable this, we first evaluated the specificity and performance of commercially available H3K27me1 antibodies (along with all other histone PTM antibodies used for ChIP in this study) with histone peptide microarrays and DNA mass measurements from ChIP enrichments (**Figure S4A-F**). We identified a single H3K27me1 antibody with robust epitope specificity, consistent chromatin mass capture across titration ranges, and concordance with histone PTM mass spectrometry profiles following VAL or TAZ treatments (**Figure S4A** and **S4F**). In contrast, other commercial H3K27me1 antibodies exhibited off-target recognition of mono-methylated epitopes and/or substantial lot-to-lot variability (**Figure S4B-C** and **S4F**).

Using this validated antibody, we performed sans spike-in quantitative chromatin immunoprecipitation sequencing (siQ-ChIP-seq) (38,39) to quantify genome-wide H3K27me1 distributions in vehicle (VEH)-, TAZ-, and VAL-treated RKO cells. Integration of these data with H3K27me3 ChIP-seq (12) and whole genome bisulfite sequencing (WGBS) data for DNA methylation (40) from the same cell line revealed that H3K27me1-enriched regions were associated with large, highly DNA methylated domains that were depleted of H3K27me3 (**Figure 4A**). Consistent with prior studies in mouse embryonic and human hematopoietic stem cells (41,42), H3K27me1 was predominantly enriched across actively transcribed gene bodies (TxWk and Tx chromHMM annotations) in RKO cells (**Figure 4B**). In contrast, H3K27me3 distributions were enriched in homogenously marked Polycomb-associated regions (ReprPCWk, ReprPC, TssBiv, EnhBiv), coinciding with partial DNA methylation and depletion of H3K27me1 (**Figure 4A-B**).

We next quantified changes in H3K27me1 distribution following EZH2-selective (TAZ) or dual EZH1/2 (VAL) inhibition. Consistent with our global analyses, siQ-ChIP-seq analysis showed that VAL treatment globally reduced H3K27me1, whereas TAZ treatment showed a redistribution of H3K27me1

that was reflected as both gains and losses (**Figure 4C**). These responses clustered into three distinct patterns of H3K27me1 redistribution, each showing strong associations with different baseline levels of H3K27me3 and DNA methylation (**Figure 4D**).

First, regions showing TAZ-specific gains in H3K27me1 were characterized by low baseline H3K27me1, high H3K27me3, and low DNA methylation levels (**Figure 4D**). These regions aligned with homogenous repressive Polycomb (ReprPC, ReprPCWk), bivalent enhancer (EnhBiv), and bivalent promoter (TssBiv) chromatin states in VEH-treated cells (**Figure 4B-C**). These data suggest that in the setting of EZH2 inhibition (and associated H3K27me2/me3 loss), EZH1 targets these canonical PRC2 domains for H3K27me1 deposition. Consistent with this model, TAZ-specific H3K27me1 gains occurred at previously identified PRC2 target loci (**Figure S5A**) and were enriched for transcription factor binding motifs (Mef2, Hox, Fox) known to be associated with EZH1 activity in the contexts of cardiac regeneration and hematopoietic stem cell differentiation (**Figure S5B**) (31,43–45).

Second, regions showing VAL-specific H3K27me1 loss (with relative retention under TAZ treatment) had intermediate baseline levels of H3K27me1, H3K27me3, and DNA methylation, suggestive of heterogenous epigenetic patterning across the RKO cell population (**Figure 4D**). These regions were enriched not only in PRC2-associated states, but also across broader repressive chromHMM annotations that include ZNF/Repeat and Heterochromatin regions (**Figure 4C**). Notably, these regions demonstrated an “epigenetic switch” between DNA methylation and H3K27me3 when DNMT1 was inhibited with the DNMT1 inhibitor GSK3484862 (**Figure 4D**), suggesting that they represent regulatory regions particularly sensitive to combined disruption of DNA methylation and PRC2 activity.

Third, shared regions that lost H3K27me1 following both TAZ and VAL treatments were characterized by high baseline H3K27me1, elevated DNA methylation, and low H3K27me3 (**Figure 4D**). These regions mapped predominantly to actively transcribed gene bodies, with a smaller fraction mapping to enhancer elements (**Figure 4C**). These regions overlapped extensively with basal H3K27me1-enriched domains in VEH-treated cells (**Figure 4B**) and exhibited comparable reductions in H3K27me1 upon either TAZ or VAL treatment (**Figure 4D**), suggesting EZH1-independent regulation of these domains.

To directly relate DNA methylation levels to EZH inhibitor-induced H3K27me1 gains and losses, we performed enzymatic methyl-sequencing (EM-seq) (46) on DNA fragments enriched by H3K27me1 ChIP (me1EM-seq). Consistent with conclusions made from integrative analysis of H3K27me1 ChIP-seq and WGBS datasets (**Figure 4A** and **4D**), me1EM-seq confirmed that H3K27me1-enriched regions were densely methylated and reflected DNA methylation patterns associated with the distinct classes of H3K27me1 redistribution described above (**Figure 4D-F**). Importantly, DNA methylation levels were unchanged by EZH inhibitor monotherapy (**Figure 4F**), and DNA methylation patterns remained highly concordant between TAZ and VAL treatments across regions of H3K27me1 redistribution (**Figure 4G**). In contrast, DNMTi treatment reduced DNA methylation across all regions of H3K27me1 redistribution (**Figure S5C**).

Collectively, these data demonstrate that H3K27me1, like DNA methylation, marks both repressive and active regions of the genome and undergoes context-dependent remodeling in response to EZH2-selective versus dual EZH1/2 inhibition (**Figure 5H**). These distinct patterns of redistribution reveal non-redundant roles for EZH1 and EZH2 in shaping the epigenomic landscape and suggest that drug-induced H3K27me1 dynamics may influence lineage-specific and developmental transcription programs through modulation of these regulatory elements.

Induced bivalency underlies cooperative gene activation by dual EZH1/2 and DNMT inhibition

Because our global analyses revealed that both EZH2-selective and dual EZH1/2 inhibitors induce gains of H3K27ac (**Figure 3H**), a PTM associated with active transcription, we next investigated how EZH inhibitor-driven redistribution of H3K27me1 relates to H3K27ac deposition and transcriptional activation of silenced genes. With a validated H3K27ac antibody (**Figure S4E**), we performed quantitative H3K27ac siQ-ChIP-seq in RKO cells treated with TAZ or VAL as monotherapy or in combination with DAC. Consistent with histone PTM mass spectrometry, EZH inhibitor treatments induced H3K27ac gains, although losses were also observed (**Figure S6A**). While DNMTi alone had marginal effects on H3K27ac, its addition with EZH inhibitors both amplified H3K27ac changes and redistributed these gains and losses across the genome relative to EZH inhibitor monotherapy (**Figure S6A-B**).

We hypothesized that loss of H3K27me1 permits p300/CBP-mediated deposition of H3K27ac, generating a therapy-induced bivalent chromatin state defined by the coexistence of activating H3K27ac and repressive DNA methylation following EZH inhibitor monotherapy. To test this hypothesis, we first focused on H3K27ac gains occurring within 10 kilobases (upstream or downstream) of H3K27me1-enriched genomic regions across treatment conditions (**Figure 5A**). VAL-specific H3K27ac gains strongly correlated with regions of H3K27me1 loss, whereas TAZ-specific H3K27ac gains occurred at regions of H3K27me1 loss and gain (**Figure 5A**).

To define the underlying DNA methylation status of H3K27ac-enriched chromatin, we performed EM-seq on DNA fragments enriched from H3K27ac ChIPs (acEM-seq). In VEH-treated cells, acEM-seq confirmed the previously reported co-existence of H3K27ac and DNA methylation at enhancers (47), whereas promoter-associated H3K27ac was largely unmethylated (**Figure S6C**). Notably, VAL monotherapy further induced this bivalent state at enhancers, with H3K27ac gains occurring over regions of established DNA methylation (**Figure 5B** and **5C**).

To further interrogate the regulatory role of H3K27me1 at these induced bivalent regions, we focused on H3K27ac gains that coincided with VAL-specific H3K27me1 depletion but TAZ-specific H3K27me1 retention or gains (**Figure 5D**). While VAL monotherapy primarily induced H3K27ac gains at enhancers, the addition of DNMTi shifted H3K27ac gains toward promoters (TssA, TssBiv) and bivalent enhancers (EnhBiv) with a modest increase in H3K27ac relative to TAZ and DAC combination (TD) treatment (**Figure 5E** and **S6D**). Motif analysis of these VAL and DAC combination (VD)-specific H3K27ac gains revealed enrichment of p53/p73 and AP-1 (Jun/Fos) transcription factor binding sites (**Figure S6E)**, consistent with prior studies linking p53/p73 to the regulation of AP-1 and EZH2i and DNMTi combination therapy to epigenetic remodeling of AP-1-associated regulatory elements (11,48).

Because many H3K27ac gains occurred at distal enhancers, we used Genomic Regions Enrichment of Annotations Tool (GREAT) to study the relationship between VAL- and VD-associated H3K27ac gains at cis-regulatory elements (CREs) and transcriptional activation (**Figure 5F-G**) (49). Both VAL- and VD-associated H3K27ac gains at CREs correlated with increased expression of linked genes (**Figure 5G**). Profiling H3K27 modifications (H3K27ac, H3K27me1, H3K27me3) at these linked CREs

(**Figure 5H**) and TSSs (**Figure 5I**) revealed that VD-responsive CREs were prone to an "epigenetic switch" between DNA methylation and H3K27me3, as DNMT1 inhibition alone resulted in compensatory accumulation of H3K27me3 (**Figure 5H**). Consistent with the model that dual EZH1/2 inhibition blocks this switch, combination treatment produced synergistic H3K27ac gains at both CREs and promoters, accompanied by robust transcriptional activation (**Figure 5H, I**). Notably, while VAL depleted H3K27me1 at these promoters, TAZ treatment resulted in retention or gain of H3K27me1 (**Figure 5I**), providing a mechanistic explanation for the superior transcriptional activation observed with VD relative to TD (**Figure 5G**).

Further supporting this model, acEM-seq analysis revealed that more than half of the H3K27ac gains induced by VAL monotherapy occurred on DNA-methylated chromatin, confirming the widespread induction of a bivalent state (**Figure 5J**). In contrast, DNMTi treatment, alone or in combination with EZHi, effectively reduced DNA methylation at both CREs and TSSs (**Figure 5K**), resolving this drug-induced bivalency. Collectively, these data support a model in which EZH inhibitor treatment induces a partially permissive, bivalent chromatin state characterized by H3K27ac deposition in the context of persistent DNA methylation, priming silenced loci for activation (**Figure 5L**). DNMT inhibition resolves this induced bivalency, enabling full enhancer- and promoter-driven gene re-expression. Importantly, dual EZH1/2 inhibition is more effective at eliminating all three states of H3K27 methylation at both enhancers and promoters, permitting robust H3K27ac deposition and transcriptional activation when combined with DNMTi.

The cancer cell-intrinsic therapeutics of combined EZHi and DNMTi are defined by suppression of p300/CBP-driven oncogenic transcription programs

We next sought to determine whether the above-described chromatin remodeling events involving EZH1-dependent H3K27me1 and p300/CBP-dependent H3K27ac are required for the antiproliferative effects of combined EZH1/2 and DNMT inhibition. To do this, we first established relevant disease-associated transcriptional programs from colorectal cancer patients. Gene set enrichment analysis (GSEA) comparing TCGA COADREAD tumors to normal tissue controls confirmed that pro-inflammatory

and innate immune pathways are downregulated in colorectal adenocarcinoma, whereas pro-survival and oncogenic gene sets, including G2/M checkpoint, MYC targets, and E2F targets, are upregulated (**Figure 6A**).

Consistent with reversal of these patient-derived signatures and our prior observations with TD in HCT116 cells (11), transcriptomic profiling showed that VD treatment robustly upregulated pathways associated with inflammation, innate immune responses, and calcium signaling in RKO cells (**Figure 6B**). To determine whether these transcriptional activation events required p300/CBP activity, we pharmacologically inhibited p300/CBP using the chemical probe A485 (50). Across a dose range that maximized target inhibition while minimizing toxicity, A485 suppressed more than 80% of VD-induced gene expression in both RKO and HCT116 cells (**Figure 6C-F** and **S7A-F**), indicating that the majority of VD-driven transcriptional activation is p300/CBP-dependent.

Despite this broad attenuation of gene activation, A485 failed to rescue the antiproliferative effects of VD (**Figure 6G** and **S7G**). Similarly, pharmacologic blockade of calcium signaling, which we previously showed attenuated pro-inflammatory and innate immune responses induced by TD in HCT116 cells (11), also failed to rescue the antiproliferative effect of combined EZH and DNMT inhibition (**Figure S7H**). These findings indicate that VD-induced transcriptional activation programs, while prominent, are not required for the cancer cell-intrinsic antiproliferative response.

Notably, both VD and A485 treatments shared a transcriptional signature characterized by downregulation of oncogenic gene sets, including MYC, E2F, and G2/M checkpoint targets (**Figure 6E-F** and **S7I**). Collectively, these data support a model in which suppression of oncogenic transcription programs, rather than induction of immune or stress-response pathways, represents a primary mechanism underlying the tumor cell-intrinsic therapeutic effect of combined EZH1/2 and DNMT inhibition.

To further test this model, and to consider the involvement of EZH1 in this regulatory mechanism, we compared transcriptional responses in EZH1-high (RKO) and EZH1-low (SW620) colon cancer cell lines (**Figure 2B**) treated with VD or TD combinations. Comparative transcriptomics analysis revealed that while VD and TD induced broadly similar patterns of transcriptional activation in both cell lines, the

magnitude of oncogenic transcriptional program repression closely tracked with therapeutic efficacy (**Figure 2C** and **6H-I).** This distinction was most evident in EZH1-high RKO cells, where TD only partially suppressed oncogenic gene sets relative to VD (**Figure 6I** and **S7J**). We validated the suppression of oncogenic gene sets at the protein level in HCT116 cells, where VD treatment reduced both c-MYC protein abundance and the expression of MYC target proteins (**Figure S7K-L**).

Collectively, these results indicate that while VAL-induced depletion of EZH1-dependent H3K27me1 enables p300/CBP-mediated chromatin activation that is required for VD-induced transcriptional activation, cancer cell-intrinsic growth suppression is more closely associated with disruption of p300/CBP-dependent support of oncogenic transcription programs. These findings establish repression of oncogenic transcription as a key determinant of cancer cell-intrinsic therapeutic efficacy of combined EZH1/2 and DNMT inhibition.

Combination DNMTi/EZHi therapy suppresses oncogenic transcription programs through coordinated loss of epigenetic features of active genes

Although histone mass spectrometry showed no global loss of H3K27ac following EZH inhibitor treatment (**Figure 3H**), we observed significant, locus-specific depletion of H3K27ac at gene promoters and genic enhancers (**Figure S6A**). Notably, EZH inhibitor-induced loss of H3K27ac at promoters of actively transcribed genes correlated with EZHi/DNMTi-induced transcriptional downregulation, an effect that was enhanced by addition of DAC (**Figure 7A**). To further define the relationship between H3K27ac loss, H3K27me1 dynamics, and transcriptional repression following treatment, we focused on VD-associated H3K27ac loss occurring within 10 kilobases of H3K27me1-enriched regions (**Figure 7B**). These events were enriched at active gene promoters (TssA) and coincided with VAL-associated depletion of H3K27me1 in adjacent chromatin regions (**Figure 7B** and **S8A**).

Analysis of H3K27me1 redistribution revealed distinct effects of EZH2-selective versus dual EZH1/2 inhibition. While VAL broadly reduced H3K27me1 across these loci (**Figure 7C**), TAZ preferentially depleted H3K27me1 within actively transcribed genic regions (TxWk, Tx, EnhG1, EnhG2) while retaining this mark at adjacent repressive chromatin domains (ReprPC, ReprCWk) (**Figure 7D**).

Despite EZHi-mediated loss of H3K27me1, DNA methylation across gene bodies was not altered and remained highly methylated in the absence of DNMT inhibition (**Figure 7E**). Consistent with these epigenomic patterns, combined EZH and DNMT inhibition preferentially downregulated genes associated with these chromatin features, with VD treatment producing a more pronounced effect than TD (**Figure 7F**). Further, enrichment analysis for HALLMARK pathways showed that these downregulated genes were enriched for oncogenic transcription programs, including G2M checkpoint, MYC targets, cell cycle, and RNA Polymerase II-associated transcription (**Figure 7G**).

Examination of core enrichment genes from GSEA analysis of these pathways demonstrated that VD treatment more effectively suppressed oncogenic transcription programs than TD (**Figure 7H**). This repression was accompanied by loss of H3K27ac at transcription start sites and depletion of H3K27me1 across gene bodies, with VAL producing deeper losses than TAZ as monotherapy or in combination with DAC (**Figure 7I-J**). These observations align with prior reports implicating EZH1 in supporting RNA polymerase II elongation at actively transcribed genes (51,52), suggesting that dual EZH1/2 inhibition disrupts this function.

Importantly, loss of H3K27ac and H3K27me1 alone with EZHi monotherapy was insufficient to induce the level of transcriptional repression observed with VD treatment (**Figure 7H-J**), indicating that additional epigenetic perturbations are required. We therefore hypothesized that DNA hypomethylation across active gene bodies contributes to suppression of oncogenic transcription. Like H3K27me1, DNA methylation levels are high across gene bodies of active genes and have been shown to regulate transcription fidelity (53). Furthermore, previous work from Yang *et al*. demonstrated that DAC-mediated DNA hypomethylation across gene bodies reduces transcriptional output, particularly of metabolic- and c-MYC-related pathways (54). Indeed, DAC as a monotherapy and in combination with EZHi induced widespread hypomethylation, including within gene bodies of actively transcribed genes (**Figure S8B**). VD-associated differentially methylated regions were enriched within highly methylated genic regions that also lost H3K27me1 following EZHi treatment (**Figure S8C**), and core oncogenic genes exhibited pronounced gene-body DNA hypomethylation under VD treatment (**Figure 7K).**

Together, these findings demonstrate that while the induction of H3K27ac deposition underlies transcriptional activation of tumor-suppressive and immune pathways, the cancer cell-intrinsic therapeutic efficacy of combined DNMTi and EZHi is driven by coordinated erosion of epigenetic features that support active oncogenic transcription. Specifically, DNA hypomethylation and H3K27me1 loss across gene bodies, coupled with H3K27ac depletion at active promoters, converge to suppress oncogenic transcription programs and limit cancer cell proliferation.

Discussion

We previously showed that EZH2 inhibition can enhance the molecular and cellular efficacy of DNMTi in colorectal cancer cells (11). Here, we extend this observation showing that dual EZH1/2 inhibition is a more effective combination. Mechanistically, our data reveal EZH1-dependent maintenance of H3K27me1 as an adaptive barrier that persists when EZH2 is genetically or pharmacologically inhibited and is uniquely removed by dual EZH1/2 inhibition. These findings provide mechanistic rationale for combining DNMT inhibitors with EZH1/2 inhibitors for solid tumor epigenetic therapy and nominate EZH1 as a biomarker to guide PRC2-targeted therapeutic strategies.

Although EZH1 and EZH2 form mutually exclusive catalytic subunits within PRC2 complexes, EZH2 is generally viewed as the dominant methyltransferase in proliferative cell states (55). Consistent with this, we show that EZH1 disruption alone in colon cancer cells has no effect on global H3K27 methylation levels. However, cancer cells with disrupted EZH2 show reduced global levels of H3K27me3 and H3K27me2 but retained or elevated levels of H3K27me1, which we show is dependent on EZH1. Mechanistically, this suggests that EZH1-containing PRC2 complexes deposit H3K27me1 to compensate for the loss of H3K27me2/me3 in transcriptionally repressed regions of the genome. This is supported by our studies mapping EZH2-selective inhibitor-dependent H3K27me1 gains to Polycomb-enriched regions (e.g., regions primarily silenced by H3K27me3).

Beyond Polycomb domains, we show that H3K27me1 also marks actively transcribed gene bodies, with enrichment toward transcription end sites that mirrors the distribution of H3.3 and other marks associated with transcription elongation (56). Notably, dual EZH1/2 inhibition depletes H3K27me1

on H3.3-containing chromatin, coinciding with repression of gene sets that define oncogenic transcription programs (e.g., MYC, E2F, G2M checkpoint). These findings are consistent with prior work implicating gene-body chromatin features, including DNA methylation and H3K27me1, in maintaining transcriptional fidelity and output (41,42), and suggest that coordinated erosion of these gene-body marks contributes to repression of oncogenic networks under combination therapy.

A key conceptual advance from this work is the identification of a therapy-induced bivalent chromatin state under EZH inhibition. Using acEM-seq, we show that EZH inhibitor monotherapy frequently produces p300/CBP-dependent H3K27ac gains on persistently DNA-methylated chromatin, particularly at enhancer elements. These regulatory elements remain silenced despite being poised for transcriptional activation. In parallel, EZH2-selective inhibition can retain or increase H3K27me1 at subsets of loci, further constraining activation. Conversely, DNMT inhibition alone promotes compensatory H3K27me3 accumulation at susceptible regions. In combination, DNMTi resolves DNA methylation-based repression and dual EZH1/2 inhibition prevents compensatory H3K27 methylation, enabling robust enhancer and promoter activation and gene re-expression.

The transcriptional programs activated by combination treatment include pathways linked to immune regulation and stress responses, raising the possibility that these cell-intrinsic changes could promote tumor-immune crosstalk *in vivo*. While our *in vitro* proliferation assays indicate that blocking p300/CBP-dependent activation does not rescue growth suppression in the absence of a tumor microenvironment, these findings do not exclude an additional immunologic contribution *in vivo*, where activation of antigen presentation, interferon-associated responses, or cytokine programs likely enhance therapeutic efficacy.

Finally, our data suggests that high EZH1 expression associates with worse outcome in COADREAD and tracks with increased dependence on dual EZH1/2 inhibition in cellular models. We speculate that elevated EZH1 supports adaptive H3K27me1 deposition that preserves repressive chromatin at key loci during EZH2 inhibition, thereby limiting the efficacy of EZH2-selective compounds. Although dual EZH1/2 inhibition shows the strongest cooperation with DNMT inhibition, EZH2-selective inhibition can still enhance DNMTi-driven activation in EZH1-high settings, potentially reflecting partial

EZH1 engagement at higher exposures. Together, these observations motivate evaluation of EZH1 abundance as a stratification biomarker and suggest that either optimal dosing or inhibitor selection (EZH2-selective vs dual) may be required to maximize therapeutic windows.

Acknowledgements

We thank members of the Rothbart laboratory and the Epigenetic Therapies SPORE for helpful discussions. We also thank Amy Johnson, Ibukunoluwa Sodiya, Hyoungjoo Lee, Colt Capan, and Molly Soper-Hopper for sample preparation, data acquisition, and analysis of proteomics data. Proteomics experiments were conducted in the Van Andel Institute's Mass Spectrometry Core (RRID:SCR_024903) with financial support from the VAI Metabolism and Nutrition (MeNu) Program (RRID:SCR_ 027494). We acknowledge support from the Van Andel Institute Genomics Core (RRID:SCR_022913) and Bioinformatics and Biostatistics Core (RRID:SCR_024762). This work was supported by grants from the National Institutes of Health to S.B.R., M.J.T., and S.B.B. (P50CA254897), A.A.C. (F32CA225043), Y.L. (F99CA305570), and a grant from the American Cancer Society to S.B.R. (RSG-21-031-01-DMC).

Methods

Cell culture

HCT116 (ATCC, CCL-247), RKO (ATCC, CRL-2577), SW620 (ATCC, CCL-227) colon cancer cell lines and HEK293T (ATCC, CRL-3216) were purchased from American Type Culture Collection (ATCC) and cultured according to ATCC recommendations. HCT116 (wild-type and the NLuc reporter line), SW620, and HEK293T were incubated at 5% CO_2 and 37°C in McCoy's (Gibco, 16600-082), Leibovitz's L-15 (ATCC, 30-2008), or DMEM (Gibco, 11995-065) culture media, respectively. RKO were maintained in RPMI 1640 (Gibco, 11875-093) culture media supplemented with L-glutamine (Gibco, 25030-081), 0.1 mM non-essential amino acids (Gibco, 11140-050), and 1 mM Sodium Pyruvate (Gibco, 11360070). All media were supplemented with 10% Fetal Bovine Serum (FBS, Millipore Sigma F0926) and 1% penicillin/streptomycin (Life Technologies, 15140-122). All cell lines were routinely tested for

mycoplasma contamination using the Venor GeM Mycoplasma Detection Kit (Sigma, MP0025-1KT) according to the manufacturer's instruction.

CRISPR/Cas9-mediated knockout cell line generation

Cloning was performed as previously reported (57). Briefly, pSpCas9(BB)-2A-Puro (PX459) V2.0 (Addgene, plasmid #62988) was digested with restriction enzyme BbsI-HF (New England Biolabs, R3539L) in rCUTSMART buffer (New England Biolabs, B6004S) and purified using Monarch Spin DNA Gel Extraction and Monarch Spin PCR & DNA Cleanup Kits (New England Biolabs, T1120S and T1130S). Oligo pairs for genes of interest (see below) were annealed and ligated into the digested vector using T4 ligase (ThermoFisher, EL0014) and transformed into XL-10 Gold ultracompetent bacterial cells (Agilent, 200315). Miniprepped plasmids (Qiagen, 27104) were confirmed by whole plasmid with Oxford Nanopore sequencing (Plasmidsaurus).

Locus	**Forward gRNA (5'-3')**	**Reverse gRNA (5'-3')**
EZH1	CACCGAGACTAAAGAAGGAGA CAGTGACA	AAACTGTCACTGTCTCCTTCT TTAGTCTC
EZH2	CACCGATCTATGTTGGGGGTA CATTCAGG	AAACCCTGAATGTACCCCCAA CATAGAT
Chr12 Gene Desert, (HG38, chr12:127711096-127713493)	CACCGTATTCCAACGGTGACT CAACCCAG	AAACCTGGGTTGAGTCACCG TTGGAATAC

Plasmids were transfected into target cell lines at a 1 µg:2 µL ratio with XtremeGene HP (Sigma, 6366244001) and selected with 2 µg/mL puromycin (Sigma, P8833) for 48 hrs. Cells were split into single cell clonal populations through limiting dilution and individual knockout clones were confirmed by western blotting for the protein of interest and Sanger sequencing (Genewiz) across the CRISPR guide target region. To analyze mutations or indels on each allele for an individual clone, we first amplified a ~400bp region around the CRISPR guide cut site (EZH2 For 5'-ACCATGCACAATATTTAGTTGGCT, EZH2 Rev 5'-TGATAGCACTCTCCAAGCTGC-3', EZH1 For 5'-GTTTTGTTAAGCAGCTCTCATTGT-3', EZH1 Rev 5'- CAGTGATCCTGGGTTTACCAGAG-3'), ligated the amplicon into a pGEM-T vector (Promega, A1360), and transformed the plasmid into JM109 cells (Promega, L2001) according to the manufacturer's guidelines. Plasmid DNA was amplified directly from bacterial colonies in 96-well plates through rolling

PCR amplification using TempliPhi according to the manufacturer's protocol (GE Healthcare, 25-6400-10) and sent for Sanger sequencing (Genewiz).

Inducible shRNA cell line generation

Inducible shRNA cell lines were generated as previously described (58,59). Briefly, the TET-pLKO-puro plasmid (Addgene, 21915) was digested with AgeI and EcoRI, and the fragment was gel purified. shRNA oligos targeting EZH1 were selected from the Broad Institute RNAi consortium shRNA library list. Oligos were ordered, annealed, and then ligated into the digested plasmid. Plasmid sequence was confirmed by Oxford Nanopore sequencing (Plasmidsaurus).

The plasmid for doxycycline-inducible shEZH1 knockdown was then transfected into HEK293T cells with pPAX2 (Addgene, 12260) and pMD2.G (Addgene, 12259) packaging plasmids to make lentivirus. RKO clones with CRISPR mutations for EZH2 (clone A8-5) or the gene desert Chr12 control (clone B2) were infected with virus media mixed with 1 mg/mL polybrene (Millipore, TR-1003-G) followed by selection with 2 µg/mL puromycin. To confirm knockdown, cells were treated with 20 ng/mL doxycycline (Cayman Chemical, 14422) for 72 hrs, collected, western blotted as below, and probed with an EZH1 antibody (Cell Signaling, 42088).

Small molecule preparation and use

Small molecules were dissolved in 100% dimethyl sulfoxide (DMSO) at 5 or 10 µM and stored at -20°C. Cells were treated with each drug or vehicle (DMSO, % equivalent) for 72-hr treatment cycles with no media change. Drugs were obtained from the following sources: 5-aza-2'-deoxycytidine (DAC or decitabine; Sigma, A3656), A485 (Cayman Chemicals, 24119), A-395 (Cayman Chemicals, 20257), CPI-169 (Selleck Chemicals, S7616), CPI-1205 (lirametostat; Selleck Chemicals, S8353), EED226 (MedChemExpress, HY-101117), Cyclosporin A (CsA; Selleck Chemicals, S2286), EEDi-5285 (MedChemExpress, HY-136977), EPZ0011989 (Selleck Chemicals, S7805), EPZ005687 (Cayman Chemical, 13966), EZH2 Degrader-2 (MedChemExpress, HY-157164), GSK126 (Selleck Chemicals, S7061), GSK343 (Selleck Chemicals, S7164), GSK503 (Cayman Chemical, 18531), MAK683

(MedChemExpress, S8983), mevrometostat (MEV or PF-1497; Chemietek, CT-PF0682), MS177 (Selleck Chemicals, E1163), MS1943 (MedChemExpress, HY-133129), ORIC-944 (Selleck Chemicals, E1967), tazemetostat (TAZ or EPZ6438; Selleck Chemicals, S7128), tulmimetostat (TUL or CPI-0209; Selleck Chemicals, E1497), UNC1999 (Caymen Chemical, 14621), valemetostat (VAL or DS-3210b; Chemietek, CT-DS3201), and UNC6852 (MedChemExpress, HY-130708).

Cell viability and longitudinal proliferation assays

To measure cell viability, cells were plated in 96-well plates at a density of 3000-4000 cells/well and treated the following day. The CellTiter-Fluor kit (Promega, G6080) was used according to the manufacturer's protocol, and fluorescence signal was measured using a BiotTek SynergyNeo2 Microplate Reader. Background signal from media-only wells was subtracted to obtain the final reported relative fluorescence units (RFU).

To measure RKO and SW620 cell longitudinal proliferation over time, cells were plated at a density of ~1000-2000 cells/well (96-well plate) or ~5000 cells/well (24-well plate) and allowed to adhere overnight. The following day, cells were treated with drugs in fresh media. Treated RKO cells were immediately placed in a Sartorius Incucyte S3 for imaging. For SW620, cells were replated and retreated a second time and directly placed in the Incucyte for imaging after an initial 72-hr treatment cycle.

To measure longitudinal proliferation of HCT116 following pretreatment, 100,000 cells/well were plated in a 6-well plate and allowed to adhere overnight. The following day, cells were treated with drugs in fresh media. After 72 hrs, cells were replated and retreated again (second treatment cycle). At six days (two 72-hr treatment cycles), 40,000 cells/well were plated into a 6-well plate and re-treated with drugs for a third and final time before being directly placed in the Incucyte for imaging.

For each well and treatment, the Incucyte captured 4 (96-well plate), 9-12 (24-well plate), or 12 (6-well plate) brightfield images per well at each timepoint. "Day 0" on each confluency graph represents the timepoint cells were placed into the Incucyte for image capture regardless of any preceding pretreatment cycles. The average confluency (%) per well and timepoint was calculated using the

Sartorius Incucyte Live Cell Imaging and Analysis software v2020C (SW620 and RKO experiments) or v2024B (all HCT116 experiments and RKO experiments with the addition of A485).

SFRP1-NanoLuciferase cell reporter assay

Engineering of the *SFRP1*-Nanoluciferase cell reporter cell line was previously reported (11). Briefly, a NanoLuciferase (NLuc) cassette was inserted into exon 2 of an endogenous *SFRP1* allele in DNMT1-hypomorph HCT116 colon cancer cells with reduced DNA methylation (19). To measure NLuc activity in *SFRP1*-NLuc reporter cells, the CellTiter-Fluor viability assay was duplexed with the Nano-Glo Luciferase Assay System (Promega, N1110). First, cells were plated and treated in 96-well plates as above for cell viability assays. To duplex the assays, CellTiter-Fluor was used at a 5x concentration preceding the Nano-Glo assay. NanoGlo reagent was applied according to the manufacturer's protocol, and a BioTek SynergyNeo2 Microplate Reader was used to obtain relative luminescence units (RLU). After background subtraction from media-only wells, RLU were normalized to CellTiter-Fluor RFU to account for cell viability.

siRNA transfection

ON-TARGETplus siRNA SMARTpools (5 µl of 20 µM stock) targeting MYC (Dharmacon, L-003282-02-0005) and non-targeting control (NTC) siRNA pools (Dharmacon, D-001810-10-05) or Lipofectamine RNAiMax (5 µL; ThermoFisher, 13778075) were each separately diluted into 100 µL Optimem (Life Technologies, 31985-062). After a 5 min separate incubation, diluted siRNA and RNAiMax were mixed together 1:1 and incubated for 20 min. McCoy's Media supplemented with 10% FBS but no antibiotics was refreshed on attached cells that had been plated the previous day at 100,000/well in a 6-well plate. The siRNA/Lipid mixture was added dropwise to the fresh media for a final siRNA concentration of 50 nM. Cells were collected 72 hrs after transfection.

Western blotting

Cells were lysed on ice in cold CSK lysis buffer as previously reported (11). 2-5 µg of total protein (to probe for histones) or 10-15 µg of total protein (for other protein targets) were size-separated by SDS-PAGE and transferred to PVDF membrane. Membranes were blocked for one hour at room temp (PBS, 0.1% Tween-20, and 5% BSA), washed in PBST (PBS supplemented with 0.1% Tween-20), and incubated in blocking buffer overnight at 4°C with the following antibodies: β-Actin (1:1,000; Cell Signaling Technology, 4970), β-Tubulin (1:50,000; Protein Tech, 66240), c-MYC (1:1000, Cell Signaling Technology, 5605), DNMT1 (1:1,000; Abcam, ab134148), EED (1:1,000; Cell Signaling Technology, 85322), EZH1 (1:1,000; Cell Signaling Technology, 42088), EZH2 (1:1,000; Cell Signaling Technology, 5246), H3 (1:50,000; EpiCypher, 13-0001), H3K18ac (1:1,000; Invitrogen, MA5-24669), H3K27ac (1:1,000; Active Motif, 39133), H3K27me1 (1:1,000; Active Motif, 61015), H3K27me2 (1:2,000; Cell Signaling Technology, 9728), and H3K27me3 (1:2,000; Cell Signaling Technology, 9733). Histone antibodies were chosen based on specificity profiling with histone peptide microarrays as previously described (60). The following day, membranes were washed in PBST and incubated in HRP-conjugated secondary antibody (1:10,000; Sigma-Aldrich, GENA934) for 1 hour at room temp, washed again in PBST, incubated in Enhanced Chemiluminescence substrate (Cytiva, 29018903), and imaged with x-ray film.

Sample preparation for histone PTM mass spectrometry

Histones were isolated by acid extraction as previously described (61). Briefly, cell pellets were lysed in hypotonic buffer (10 mM Tris–HCl pH 8.0, 1 mM KCl, 1.5 mM $MgCl_2$, 1 mM DTT, 1 mM PMSF, 5 mM sodium butyrate, EDTA-free Roche mini protease inhibitor tablet (Sigma, 11836170001), and PhosSTOP Phosphatase Inhibitor tablet (Sigma, 4906837001) with rotation at 4°C for 30 min. Nuclei were then pelleted by centrifugation at 10,000 g for 10 min at 4°C, resuspended in cold 0.2 M H_2SO_4, rotated at 4°C for 2-4 hrs, and centrifuged at 16,000 g for 10 min at 4°C. Histones in the soluble fraction were precipitated by dropwise addition of cold trichloroacetic acid (33% v/v) followed by incubation with rotation at 4°C for at least 1 hr. Precipitated histones were pelleted by centrifugation at 16,000 g for 10 min at 4°C, washed with cold acetone in 0.1% HCl, pelleted again at 3,400 g for 5 min at 4°C, and washed

again with cold acetone. A glass Pasteur pipette was used to gently wash precipitates that collected on the sides of tubes during spin steps. Samples were air-dried for 20 min on the benchtop before proceeding to chemical derivatization and digestion steps.

Acid extracted histones were propionylated by chemical derivatization as previously described (12,62) or with the following procedural modifications. Purified histones were resuspended in 100 mM ammonium bicarbonate (Sigma, 09830) with 20% acetonitrile (Fisher Chemical, LC/MS grade) at 25 µg histone/µL, propionylated with 5 µL ≥99% propionic anhydride (Sigma, 240311) immediately followed by the addition of 10 µL 20-22% ammonium hydroxide (Fisher, A470), pH was adjusted to ~8.0 with additional propionic anhydride or ammonium hydroxide, and incubated for 10 min at 25°C. Propionylation was repeated once more before overnight tryptic digestion at a ratio of 50:1 histone:trypsin (Promega, V5073). After overnight digestion, samples were propionylated two more times as before and dried in a vacuum concentrator (Genevac, SpeedVac). Digests were cleaned using an Ultra-Micro C18 Spin Column (Harvard Apparatus, 74-7206), dried, and resuspended at a concentration of 1 µg/µL in 0.1% trifluoroacetic acid (TFA; Sigma, T6508) prior to mass spectrometry analysis.

Data-independent acquisition (DIA) LC-MS/MS proteomics for histones and their PTMs

DIA analyses were performed on Orbitrap Exploris 480 coupled to Vanquish Neo system (Thermo Fisher Scientific). 1 µg of digested propionylated peptides were separated on a nano capillary liquid chromatography (LC) column (20 cm × 75 µm I.D., 365 µm O.D., 1.7 µm C18, CoAnn Technologies #HEB07502001718IWF) at a flow rate of 300 nL/min. Mobile phase A consisted of 0.1% formic acid (FA) in LC/MS-grade H_2O (Fisher Scientific, LS118- 500) and mobile phase B consisted of 80% LC/MS-grade acetonitrile (Fisher Scientific, LS122500) and 0.1% FA in LC/MS-grade H_2O. The LC gradient was: 3% B to 30% B over 51 min, 80% B over 5 min, 98% B over 2 min, and a hold at 98% B for 3 min, with a total gradient time of 60 min. Column temperature was kept constant at 45 °C using a customized column heater (Phoenix S&T). Full MS spectra were collected at 120,000 resolution (full width half-maximum; FWHM), and MS2 spectra at 30,000 resolution (FMWH). Both the standard automatic gain control (AGC) target and the automatic maximum injection time were selected. A precursor range of 300-1000 m/z was

set for MS2 scans, and an isolation window of 30 m/z was chosen with a 1 m/z overlap for each scan cycle. 32% HCD collision energy was used for MS2 fragmentation. DIA data was processed in EpiProfile (version 2.1) (63) using the manufacturer's default parameters.

Sample Preparation for untargeted global proteomics

Samples were processed using the EasyPep Maxi MS Sample Prep Kit (Thermo Fisher Scientific, A45734) according to the manufacturer's protocol. Briefly, up to $2X10^7$ cells were resuspended in 50 µL of lysis buffer and proteins were quantified using the Pierce BCA Protein Assay Kit (Thermo Fisher Scientific, 23227) following the manufacturer's protocol. Plates were read at an absorbance of 562 nm using a Synergy LX Multi-Mode Reader, and Gen5 software was used for data analysis (BioTek/Agilent). Polynomial regression was used in the Gen5 software to calculate protein concentrations to a protein standard curve after an average blank absorbance subtraction. 25 µg of protein per sample was then reduced and alkylated at 95ºC for 10 min, and samples were digested overnight with Trypsin/Lys-C at 30ºC at a ratio of 10:1 (protein:enzyme (w/w)). Resulting peptides were cleaned with EasyPep Maxi kit peptide clean up columns and dried down in a vacuum concentrator. Samples were resuspended in 12.5 µL 0.1% FA (Fisher Scientific, LS118-1) and diluted 1:1 with 6 µL of 0.1% TFA (Fisher Scientific, LS119-500) in autosampler vials.

Data-independent acquisition (DIA) LC-MS/MS for untargeted global proteomics

DIA analyses were performed on an Orbitrap Eclipse coupled to a Vanquish Neo system (Thermo Fisher Scientific) with a FAIMS Pro source (Thermo Fisher Scientific) located between the nanoESI source and the mass spectrometer.

Digested peptides (2 µg) were separated on a nano capillary column (20 cm × 75 µm I.D., 365 µm O.D., 1.7 µm C18, CoAnn Technologies #HEB07502001718IWF) at a flow rate of 300 nL/min. Mobile phase A consisted of 0.1% FA in LC/MS grade H_2O (Fisher Scientific, LS118- 500) and mobile phase B consisted of 80% LC/MS grade acetonitrile (Fisher Scientific, LS122500) and 0.1% FA in in LC/MS grade

H_2O. The LC gradient was: 1% B to 24% B over 110 min, 85% B over 5 min, and 98% B over 5 min, with a total gradient time of 120 min.

The column temperature was kept constant at 50 °C using a customized column heater (Phoenix S&T). For FAIMS, the selected compensation voltage (CV) was applied (−40V, -55V, and -70V) throughout the LC-MS/MS runs. Full MS spectra were collected at 120,000 resolution (full width half-maximum; FWHM), and MS2 spectra at 30,000 resolution (FMWH). Both the standard automatic gain control (AGC) target and the automatic maximum injection time were selected. A precursor range of 380-985 m/z was set for MS2 scans, and an isolation window of 50 m/z was chosen with a 1 m/z overlap for each scan cycle. 32% HCD collision energy was used for MS2 fragmentation.

DIA data were processed in Spectronaut (version 18, Biognosys) using direct DIA. Data were searched against the *Homo sapiens* proteome. The manufacturer's default parameters were used. Briefly, trypsin/P was set as the digestion enzyme, and two missed cleavages were allowed. Cysteine carbamidomethylation was set as a fixed modification, and methionine oxidation and protein N-terminus acetylation as variable modifications. Identification was performed using a 1% q-value cutoff on precursor and protein levels. Both peptide precursors and protein false discovery rate (FDR) were controlled at 1%. Ion chromatograms of fragment ions were used for quantification. For each targeted ion, the area under the curve between the XIC peak boundaries was calculated.

Chromatin preparation

Cells were fixed in 1% formaldehyde in Dulbecco's phosphate-buffered saline (DPBS) without calcium or magnesium (Gibco, 14190-144) 10 min at 25ºC with shaking, quenched with 125 mM glycine for 5 min at room temp, scraped into cold DPBS, washed 2X with cold DPBS, flash frozen in liquid nitrogen, and stored at -80°C until use. Thawed pellets were lysed in 1 mL cell lysis buffer (5 mM PIPES pH 8.0, 85 mM KCl, 1% NP40, 100 mM PMSF, Roche EDTA-free protease inhibitor cocktail) for 20 min with rotation at 4°C and cleared by centrifugation at 2000 x g for 5 min at 4°C. Pelleted nuclei were washed in cold Micrococcal nuclease (Mnase) digestion buffer (50 mM Tris-HCl pH 8.0, 1 mM $CaCl_2$, 300 mM sucrose, 100 mM PMSF, Roche EDTA-free protease inhibitor cocktail), pelleted by centrifuge,

resuspended in 1 mL 37°C Mnase buffer with 50U Mnase (Worthington, LS004798), and incubated at 37°C shaking vigorously for 12 min. Digestion was stopped by addition of 10 mM EDTA and nuclei were transferred to a 1 mL milliTUBE (Covaris). Chromatin was sheared to a range of 300-600 base-pair fragments using a Covaris E220 evolution Focused ultrasonicator with the following parameters: Peak power (140.0), Duty Factor (5.0), Cycles/Burst (200), Duration (120 seconds), Temperature (4°C). Samples were centrifuged at 13,000 rpm at 4°C for 10 min and supernatants collected and stored at –80°C.

To quantify chromatin, 20 µL of the above-digested chromatin was diluted in 80 µL elution buffer (50 mM $NaHCO_3$, 1% SDS), 0.3 M NaCl, and 200 µg/mL proteinase K. Samples were incubated at 67°C overnight to reverse crosslinks and remove protein, followed by incubation with RNase A/T (Invitrogen EN0551) at 37°C for 30 min to remove RNA. DNA was purified using the Qiagen PCR purification kit (Qiagen, 28104) and quantified by Qubit dsDNA High Sensitivity kit (Invitrogen, Q32854). Correct DNA fragment size was confirmed by 2% agarose gel electrophoresis.

Antibody validation for chromatin immunoprecipitation

Antibodies were analyzed for binding specificity using histone peptide arrays as previously described (60,64). Briefly, streptavidin-coated glass microscope slides that displayed a printed library of biotinylated singly- and combinatorially-modified (primarily methylation, acetylation, and phosphorylation) histone peptides were blocked with in hybridization buffer (1X PBS pH 7.6, 0.1% Tween, 5% BSA) followed by primary antibody hybridization. Following washing and hybridization of an Alexa Fluor 647 conjugated secondary antibody (1:5000; Life technologies, A21245), slides were scanned with an Innoscan 1100AL microarray scanner (Innopsys). Binding profiles were then analyzed using ArrayNinja (65) (**Figure S4**).

Chromatin enrichment analysis with antibody titrations was performed as previously described (39) with a fixed amounts of chromatin prepared as above (equivalent to 5 µg quantified DNA) and incubated with increasing amounts of antibody. Chromatin was immunoprecipitated with antibodies as below and total DNA mass quantified (**Figure S4**).

Chromatin Immunoprecipitation (ChIP)

For immunoprecipitation, prepared chromatin (equivalent to 5 µg quantified DNA) was incubated with either 2.5 µL (2.5 µg) of H3K27ac antibody (ActiveMotif, 39133, lot 31521015) or 5 µL of H3K27me1 antibody (ActiveMotif, 61015, lot 03822017) overnight at 4°C with constant rotation. 5% input of normalized chromatin was removed and set aside. The next day, 30 µL of Dynabeads Protein G magnetic beads (ThermoFisher, 10004D) was added and samples were incubated for 3 hours at 4°C with rotation. Bead-immuno-chromatin complexes were then washed 3X for 5 min with rotation at room temperature with low salt WB1 (20 mM Tris-HCl pH 8.0, 150 mM NaCl, 2 mM EDTA, 1% Triton X-100, 0.1% SDS), 3X with high salt WB2 (20 mM Tris-HCl pH 8.0, 500 mM NaCl, 2 mM EDTA, 1% Triton X-100, 0.1% SDS), 1X with WB3 (20 mM Tris-HCl pH 8.0, 250 mM LiCl, 1 mM EDTA, 1% NP-40, 1% Na-deoxycholate) and 1X with TE (10 mM Tris-HCl pH 8.0, 1 mM EDTA pH 8.0). Beads were incubated in 100 µl of elution buffer shaking at 65°C for 30 min to elute immuno-chromatin complexes. Reverse crosslinking, protein digestion, RNA digestion, and DNA clean up were performed as above for both the IPs and the input samples to both quantify and isolate DNA for sequencing.

siQ-ChIP library preparation and sequencing

Immunoprecipitated fragments and saved inputs were quantified with a Qubit dsDNA High Sensitivity Assay kit (Invitrogen, Q32851), and 10 ng of purified DNA for each IP and input sample were used for library preparation with the KAPA Hyper Prep Kit (Kapa Biosystems, KR0961). Library preparation, including fragment end-repair, A-tail extension, and adapter ligation, was conducted per the manufacturer's instructions (KAPA). Adapter-ligated fragments were amplified with 11 cycles of PCR following the recommended thermocycler program, and DNA was purified with two rounds of purification using KAPA Pure Beads (KK8000). Quality and quantity of prepped libraries were assessed using a combination of Agilent DNA High Sensitivity chip (Agilent Technologies, Inc.), QuantiFluor® dsDNA System (Promega), and Kapa Illumina Library Quantification qPCR assays (Kapa Biosystems).

Individually indexed libraries were pooled, and 50 bp paired end sequencing was performed on an Illumina NovaSeq6000 sequencer using an S2 100 bp sequencing kit to a minimum read depth of 50M read pairs per IP library and 100M read pairs per Input library. Base calling was done by Illumina RTA3 and output of NCS was demultiplexed and converted to FastQ format with Illumina Bcl2fastq (v1.9.0).

siQ-ChIP-seq processing and analysis

siQ-ChIP sequencing reads were 3' trimmed and filtered for quality and adapter content using TrimGalore (v0.5.0) and quality was assessed by FastQC (v0.11.8). Reads were aligned to human assembly hg38 with bowtie2 (v2.3.5, RRID:SCR_016368) and were deduplicated using removeDups from samblaster (v.0.1.24) (66). Aligned BAM files were used for quality control analysis with "deeptools" (v3.5.4), 'plotFingerprint,' and 'plotPCA' functions. Aligned SAM files were then processed for pair-end reads with high mapping quality (MAQ ≥ 20), correct pair orientation (Sam Flags = 99, 163), and fragment length as described for siQ-ChIP (https://github.com/BradleyDickson/siQ-ChIP). Param.in files were prepared for each sample with all required parameters and measurements required for siQ-ChIP normalization. IP tracks (with siQ-ChIP efficiency values) and comparative responses between drug treatments (relative to VEH) were generated with execution of getsiq.sh (version: September 2024) with the EXPlayout file (NOTE: params.in files will be provided with the GEO accession). Each individual inhibitor-treated biological replicate was compared to each individual vehicle-treated biological replicate.

To determine changes in H3K27ac distributions between inhibitor-treated samples and vehicle-treated samples, each inhibitor-treated biological replicate (e.g., DAC1) was individually compared to VEH-treated biological replicates (e.g., DAC1 vs. Veh1, DAC1 vs. Veh2, etc.), and the average $\log_2$ fold-change in response (area of peak in inhibitor treatment/area of peak in vehicle treatment) was calculated. Peaks were considered conserved among biological replicates using the GenomicRanges (v1.56.2) 'findOverlaps' function. Finally, average $\log_2$ fold-changes in responses were calculated for peaks conserved between the two inhibitor-treated biological replicates. For H3K27ac, peaks were considered significant if the $\log_2$ fold-change in response was ≥ 0.585 (increase) or ≤ -1.0 (decrease). For H3K27me1,

the variance (in general high among the 3 biological replicates) (≤ 1) was considered for significance peak calling along with $\log_2$ fold-change ≤ -0.5 (decrease) or ≥ 0.5 (increase).

ChromHMM (v1.23)

Enrichment overlap analysis with siQ-ChIP-quantified peaks were conducted with the 'OverlapEnrichment' function using the genomic coordinates for each dataset and the publicly available 18-state chromHMM annotation for parental RKO cells (ENCODE ENCSR974TXE) (67). Enrichment bias for chromHMM states across individual sample analyses were calculated as the percent enrichment for a particular state divided by the total enrichment across all chromHMM states. 18-state chromHMM annotations were condensed into general genomic annotation categories as follows: Promoter (TssA, TssFlnk, TssFlnkD, TssFlnkU, TssBiv), Enhancer (EnhBiv, EnhA1, EnhA2, EnhWk, EnhG1, EnhG2), Genic (TxWk, Tx), and Repressive (ReprPCWk, ReprPC, Het, Quies, ZNF/Rpts).

Enzymatic-Methyl-seq (EM-seq) library preparation and sequencing

Libraries were prepared by the Van Andel Institute Genomics Core (RRID:SCR_022913) from an input of 41 to 51 ng of ChIP DNA (taken directly from DNA immunoprecipitated for siQ-ChIP-seq) using the NEBNext EM-seq Kit (New England Biolabs, E7120L). The denaturation method used was 0.1 N of sodium hydroxide, according to the protocol, and 8 cycles of PCR amplification were performed. Quality and quantity of the finished libraries were assessed using a combination of the Agilent High Sensitivity DNA chip (Agilent Technologies Inc., 5067-4626) and QuantiFluor dsDNA System (Promega, E2670). Paired-end sequencing (150 bp) was performed on an Illumina NovaSeq6000 sequencer using an S4, 300-bp sequencing kit (Illumina Inc.), with 10% PhiX to a minimum read depth of 100 M read pairs per library. Base calling was done by Illumina RTA3, and output of NCS was demultiplexed and converted to FastQ format with Illumina Bcl2fastq (v1.9.0).

EM-seq processing and analysis

EM-seq reads were aligned to human genome build hg38, duplicate-marked (samblaster, RRID:SCR_000468), and sorted (samtools, RRID:SCR_002105) using the "biscuitBlaster" pipeline from BISCUIT (v1.7.1) (https://huishenlab.github.io/biscuit/). Cytosine retention and callable single-nucleotide polymorphism mutations were computed with "biscuit pileup" and output into a VCF file. Cytosine 5mC-values and coverage were extracted with "biscuit vcf2bed" and CpG methylation status was merged with "biscuit mergecg." CpH dinucleotides (control for EM conversion) showed less than 0.5% cytosine methylation indicating that we achieved >99% conversion efficiency on all EM-seq libraries.

CpGs covered by at least 3 reads were retained in downstream analysis for each individual acEM-seq and me1EM-seq sample library. 5mC-values for individual CpGs were converted to bigwig format using UCSC tools (v2.1) (68). Integrated siQ-ChIP-seq and EM-seq analysis was conducted with deeptools (v3.5.4) (69) by constructing matrices with 'computeMatrix' across queried genomic coordinates with the respective bigwig data and visualizing the summarized integration with 'plotProfile' and 'plotHeatmap'.

Genomic DNA isolation

Genomic DNA was extracted using the DNeasy Blood & Tissue Kit (Qiagen, 69504) following the standard protocol. Samples were then treated with 1 mg/ml RNAse A at 37°C for 30 minutes. DNA was re-precipitated with 1/10 volume 3 M sodium acetate pH 4.8 and 2.5 volumes 100% ethanol and stored overnight at -20°C. Precipitated DNA was pelleted by centrifugation at 17,090 g for 30 minutes at 4°C. The pelleted DNA was washed twice with 70% ethanol, allowed to dry for 15 minutes, and resuspended in nuclease-free water.

Infinium MethylationEPIC BeadChip (EPIC array)

Genomic DNA was quantified with the Qubit dsDNA High Sensitivity Assay kit (Invitrogen, Q32851), and 1.5 µg of genomic DNA was submitted to the VAI Genomics Core (RRID:SCR_022913) for quality control analysis, bisulfite conversion, and DNA methylation quantification using the Infinium

MethylationEPIC BeadChIP (Illumina) processed on an Illumina iScan system following the manufacturer's standard protocol (70,71).

EPIC array data processing and analysis

All analyses were conducted in the R statistical software (v4.4.1) (R Core Team). Raw IDAT files for each sample were processed using the Bioconductor (RRID:SCR_006442) package "SeSAMe" (version 1.22.2) for extraction of probe signal intensity values, normalization of probe signal intensity values, and calculation of β-values from the normalized probe signal intensity values (72). The β-value is the measure of DNA methylation for each individual CpG probe, where a minimum value of 0 indicates a fully unmethylated CpG and a maximum value of 1 indicates a fully methylated CpG in the population. CpG probes with a detection p-value > 0.05 in any one sample were excluded from the analysis. Differentially methylated regions (DMRs) were called using the Bioconductor package "DMRcate" (v3.0.10), and regions were considered differentially methylated if at least five contiguous CpGs demonstrated a mean difference of 0.20 methylation change in drug-treated cells compared to vehicle (VEH)-treated cells.

Construction and sequencing of directional total RNA-seq libraries

Libraries were prepared by the Van Andel Institute Genomics Core (RRID:SCR_022913) from 500 ng of total RNA using the KAPA RNA HyperPrep Kit (Kapa Biosystems). Ribosomal RNA material was reduced using the QIAseq FastSelect –rRNA HMR Kit (Qiagen). RNA was sheared to 300-400 bp. Prior to PCR amplification, cDNA fragments were ligated to IDT for Illumina TruSeq UD Indexed adapters (Illumina Inc). Quality and quantity of the finished libraries were assessed using a combination of Agilent DNA High Sensitivity chip (Agilent Technologies, Inc.) and QuantiFluor® dsDNA System (Promega). Individually indexed libraries were pooled, and 50 bp paired end sequencing was performed on an Illumina NovaSeq6000 sequencer to an average depth of 50M raw paired-reads per transcriptome. Base calling was done by Illumina RTA3 and output of NCS was demultiplexed and converted to FastQ format with Illumina Bcl2fastq (v1.9.0).

RNA-seq processing and analysis

Raw 50 bp paired-end reads were trimmed with TrimGalore! (http://www.bioinformatics.babraham.ac.uk/projects/trim_galore/) (RRID:SCR_011847) followed by quality control analysis with FastQC. Trimmed reads were aligned to GRCh38.p12 and indexed to GENCODE v29 via STAR (v2.5.3a) aligner with flags '-twopassMode Basic\ -quantMode GeneCounts' for feature counting.

ReadsPerGene output count files were constructed into a raw read count matrix in R. Low count genes were filtered (1 count in at least one sample) prior to edgeR (v4.2.2) count normalization and differential expression analysis with voomWithQualityWeights and quasi-likelihood fit set to robust. Principal component analysis was calculated using 'prcomp' in the R stats package on the normalized expression matrix. Differential expression analysis was conducted with voomWithQualityWeights and a quasi-likelihood fit set to robust. Each dataset was treated separately for differential expression analysis, and all inhibitor treatments were compared to their respective vehicle samples. Genes were considered differentially expressed if $|\log_2 FC| \geq 1$ and FDR ≤ 0.01.

Gene Set Enrichment Analysis (GSEA)

GSEA (v4.3.3) (73) was conducted across the HALLMARK and c2.cp.kegg curated gene set databases from Molecular Signature Database (MSigDB). Phenotype comparisons were set to the sample of interest (e.g., VD) VS REST (monotherapy treatments; e.g., VEH/DAC/VAL) for all analyses with weighted enrichment statistic and Signal2Noise settings for ranking genes. Maximum and minimum size of a gene set was defined as 1500 and 15 genes, respectively. Genes marked as a "core enrichment" gene were used for epigenetic profiling and heatmap row z-score analysis of normalized cpm values.

Integrative genomic analysis

As described in the respective sections above, bigwig files were generated for each sample for genome-wide H3K27ac and H3K27me1 efficiency (siQ-ChIP-seq), DNA methylation β-values (EPIC

array), and publicly available datasets for RKO parental Whole Genome Bisulfite Sequencing (GSE262054, WGBS) (74) and our previously published H3K27me3 siQ-ChIP data (GSE256135) for parental- and DNMT1i- (GSK3484862, 1 μM) treated RKO cells (12). Bed files with genomic coordinates for differential H3K27 peak analysis and ChromHMM chromatin state annotations were generated as described above. Integrated siQ-ChIP-seq, WGBS, and EPIC array analysis was conducted with deeptools (v3.5.4) (69) by constructing matrices with 'computeMatrix' across queried genomic coordinates with the respective bigwig data and visualizing the summarized integration with 'plotProfile' and 'plotHeatmap'. Motif enrichment analysis was conducted using 'findMotifsGenome.pl -len 8,10,12' from HOMER (v4.11.1) (75).

TCGA COADREAD patient data

Colorectal adenocarcinoma (COADREAD) TCGA patient data was accessed via the UCSC Xena Genome Browser (76). EZH1 and EZH2 normalized mRNA expression data was processed with patient survival outcomes using survival (https://github.com/therneau/survival, v3.8-3) and survminer (https://github.com/kassambara/survminer, v.0.5). Gene set enrichment analysis was conducted on patient samples using the Xena Browser plug-in for blizGSEA (https://github.com/MaayanLab/blitzgsea) (77).

Data and Code Availability

All sequencing and EPIC array data have been deposited to the Gene Expression Omnibus (GEO) under the following accession numbers: ChIP-seq (GSE320400), EM-seq (GSE320401), EPIC-array (GSE320533), RNA-seq (GSE320534). Final code used for bioinformatic analysis will be deposited on our GitHub page and archived with Zenodo prior to publication.

Recombinant nucleosome preparation

Recombinant mononucleosomes were reconstituted as previously described (78). Briefly, *Xenopus laevis* histones H2A, H2B, H3, and H4 were purchased from The Histone Source (Colorado

State University). Lyophilized histones were resuspended in unfolding buffer (20 mM Tris-HCl pH 7.5, 7 M guanidine-HCl, and 10 mM DTT). Octamers were assembled by mixing histones H2A/H2B/H3/H4 and dialyzing into refolding buffer (10 mM Tris-HCl pH 7.5, 2 M NaCl, 1 mM EDTA, 5 mM BME) at 4°C, then purified by size exclusion chromatography using a Superdex 200 column (Cytiva). 175 bp DNA templates were generated by PCR amplification of the 147x601 Widom nucleosome positioning sequence and purified by ion exchange chromatography using a RESOURCE Q column (Cytiva). Octamers and DNA templates were mixed and assembled into nucleosomes via an 18-hour dialysis from RB high (10 mM Tris-HCl pH 7.5, 2 M KCl, 1 mM EDTA, and 1 mM DTT) to RB low (10 mM Tris-HCl pH 7.5, 250 mM KCl, 1 mM EDTA, and 1 mM DTT) at 4°C.

In vitro PRC2 activity assays

Recombinant PRC2 complexes comprising SUZ12, EED, RbAp46, and RbAp48 with EZH1 or EZH2 were purchased (Active Motif, 31500 and 31387, respectively). PRC2 activity assays containing 20 nM PRC2 complex, 750 nM recombinant nucleosome substrate from above, 20 μM SAM, and inhibitor or vehicle (DMSO) were assembled in reaction buffer (20 mM Tris-HCl pH 8, 50 mM NaCl, 1 mM EDTA, 3 mM $MgCl_2$, and 0.1 mg/mL BSA) in a final volume of 10 μL. Reactions were incubated at room temp overnight, then quenched by adding TFA to 0.5% v/v. PRC2 activity was measured using the MTase-Glo Methyltransferase Assay (Promega, V7601) according to the manufacturer's instructions. IC_{50} values were generated by non-linear regression analysis using GraphPad Prism (RRID:SCR_002798).

References

1. Hanahan D. Hallmarks of Cancer: New Dimensions. Cancer Discov. 2022;12:31–46.
2. Esteller M, Dawson MA, Kadoch C, Rassool FV, Jones PA, Baylin SB. The Epigenetic Hallmarks of Cancer. Cancer Discov. 2024;14:1783–809.
3. Mabe NW, Perry JA, Malone CF, Stegmaier K. Pharmacological targeting of the cancer epigenome. Nat Cancer. Nature Publishing Group; 2024;5:844–65.
4. Chiappinelli KB, Strissel PL, Desrichard A, Li H, Henke C, Akman B, et al. Inhibiting DNA Methylation Causes an Interferon Response in Cancer via dsRNA Including Endogenous Retroviruses. Cell. 2015;162:974–86.
5. Roulois D, Loo Yau H, Singhania R, Wang Y, Danesh A, Shen SY, et al. DNA-Demethylating Agents Target Colorectal Cancer Cells by Inducing Viral Mimicry by Endogenous Transcripts. Cell. 2015;162:961–73.
6. Gore SD, Jones C, Kirkpatrick P. Decitabine. Nat Rev Drug Discov. Nature Publishing Group; 2006;5:891–2.
7. Issa J-P, Kantarjian H. Azacitidine. Nat Rev Drug Discov. 2005;Suppl:S6-7.
8. Feng S, De Carvalho DD. Clinical advances in targeting epigenetics for cancer therapy. FEBS J. 2022;289:1214–39.
9. Diesch J, Zwick A, Garz A-K, Palau A, Buschbeck M, Götze KS. A clinical-molecular update on azanucleoside-based therapy for the treatment of hematologic cancers. Clin Epigenetics. 2016;8:71.
10. Dai W, Qiao X, Fang Y, Guo R, Bai P, Liu S, et al. Epigenetics-targeted drugs: current paradigms and future challenges. Signal Transduct Target Ther. Nature Publishing Group; 2024;9:332.
11. Chomiak AA, Tiedemann RL, Liu Y, Kong X, Cui Y, Wiseman AK, et al. Select EZH2 inhibitors enhance viral mimicry effects of DNMT inhibition through a mechanism involving NFAT:AP-1 signaling. Sci Adv. 2024;10:eadk4423.
12. Liu Y, Hrit JA, Chomiak AA, Stransky S, Hoffman JR, Tiedemann RL, et al. DNA hypomethylation promotes UHRF1-and SUV39H1/H2-dependent crosstalk between H3K18ub and H3K9me3 to reinforce heterochromatin states. Mol Cell. 2024;S1097-2765(24)00914-6.
13. Deblois G, Tonekaboni SAM, Grillo G, Martinez C, Kao YI, Tai F, et al. Epigenetic Switch-Induced Viral Mimicry Evasion in Chemotherapy-Resistant Breast Cancer. Cancer Discov. 2020;10:1312–29.
14. Dimopoulos K, Helbo AS, Munch-Petersen HF, Sjö L, Christensen J, Kristensen LS, et al. Dual inhibition of DNMTs and EZH2 can overcome both intrinsic and acquired resistance of myeloma cells to IMiDs in a cereblon-independent manner. Mol Oncol. 2018;12:180–95.
15. Wang S, C. Ordonez-Rubiano S, Dhiman A, Jiao G, Strohmier BP, Krusemark CJ, et al. Polycomb group proteins in cancer: multifaceted functions and strategies for modulation. NAR Cancer. 2021;3:zcab039.
16. Kim KH, Roberts CWM. Targeting EZH2 in cancer. Nat Med. 2016;22:128–34.
17. Rothbart SB, Baylin SB. Epigenetic Therapy for Epithelioid Sarcoma. Cell. 2020;181:211.
18. Morin RD, Arthur SE, Assouline S. Treating lymphoma is now a bit EZ-er. Blood Adv. 2021;5:2256–63.
19. Egger G, Jeong S, Escobar SG, Cortez CC, Li TWH, Saito Y, et al. Identification of DNMT1 (DNA methyltransferase 1) hypomorphs in somatic knockouts suggests an essential role for DNMT1 in cell survival. Proc Natl Acad Sci U S A. 2006;103:14080–5.
20. Keller PJ, Adams EJ, Wu R, Côté A, Arora S, Cantone N, et al. Comprehensive Target Engagement by the EZH2 Inhibitor Tulmimetostat Allows for Targeting of ARID1A Mutant Cancers. Cancer Res. 2024;84:2501–17.
21. Lakhani NJ, Gutierrez M, Duska LR, Do KT, Sharma M, Gandhi L, et al. Phase 1/2 first-in-human (FIH) study of CPI-0209, a novel small molecule inhibitor of enhancer of zeste homolog 2 (EZH2) in patients with advanced tumors. J Clin Oncol. Wolters Kluwer; 2021;39:3104–3104.
22. Honma D, Kanno O, Watanabe J, Kinoshita J, Hirasawa M, Nosaka E, et al. Novel orally bioavailable EZH1/2 dual inhibitors with greater antitumor efficacy than an EZH2 selective inhibitor. Cancer Sci. 2017;108:2069–78.

23. Keam SJ. Valemetostat Tosilate: First Approval. Drugs. 2022;82:1621–7.
24. Izutsu K, Makita S, Nosaka K, Yoshimitsu M, Utsunomiya A, Kusumoto S, et al. An open-label, single-arm phase 2 trial of valemetostat for relapsed or refractory adult T-cell leukemia/lymphoma. Blood. 2023;141:1159–68.
25. Schweizer MT, Calvo M, Moreno V, Mellado B, Castellano D, Spira AI, et al. Mevrometostat (PF-06821497), an enhancer of zeste homolog 2 (EZH2) inhibitor, in combination with enzalutamide in patients with metastatic castration-resistant prostate cancer (mCRPC): A randomized dose-expansion study. J Clin Oncol. Wolters Kluwer; 2025;43:LBA138–LBA138.
26. Kung P-P, Bingham P, Brooun A, Collins M, Deng Y-L, Dinh D, et al. Optimization of Orally Bioavailable Enhancer of Zeste Homolog 2 (EZH2) Inhibitors Using Ligand and Property-Based Design Strategies: Identification of Development Candidate (R)-5,8-Dichloro-7-(methoxy(oxetan-3-yl)methyl)-2-((4-methoxy-6-methyl-2-oxo-1,2-dihydropyridin-3-yl)methyl)-3,4-dihydroisoquinolin-1(2H)-one (PF-06821497). J Med Chem. American Chemical Society; 2018;61:650–65.
27. Zinzani PL, Izutsu K, Mehta-Shah N, Barta SK, Ishitsuka K, Córdoba R, et al. Valemetostat for patients with relapsed or refractory peripheral T-cell lymphoma (VALENTINE-PTCL01): a multicentre, open-label, single-arm, phase 2 study. Lancet Oncol. 2024;25:1602–13.
28. Margueron R, Li G, Sarma K, Blais A, Zavadil J, Woodcock CL, et al. Ezh1 and Ezh2 Maintain Repressive Chromatin through Different Mechanisms. Mol Cell. 2008;32:503–18.
29. Lavarone E, Barbieri CM, Pasini D. Dissecting the role of H3K27 acetylation and methylation in PRC2 mediated control of cellular identity. Nat Commun. Nature Publishing Group; 2019;10:1679.
30. Lee C-H, Holder M, Grau D, Saldaña-Meyer R, Yu J-R, Ganai RA, et al. Distinct Stimulatory Mechanisms Regulate the Catalytic Activity of Polycomb Repressive Complex 2. Mol Cell. 2018;70:435-448.e5.
31. Xu J, Shao Z, Li D, Xie H, Kim W, Huang J, et al. Developmental control of polycomb subunit composition by GATA factors mediates a switch to non-canonical functions. Mol Cell. 2015;57:304–16.
32. Honer MA, Ferman BI, Gray ZH, Bondarenko EA, Whetstine JR. Epigenetic modulators provide a path to understanding disease and therapeutic opportunity. Genes Dev. Cold Spring Harbor Lab; 2024;38:473–503.
33. Porazzi P, Nason S, Yang Z, Carturan A, Ghilardi G, Guruprasad P, et al. EZH1/EZH2 inhibition enhances adoptive T cell immunotherapy against multiple cancer models. Cancer Cell. Elsevier; 2025;43:537-551.e7.
34. Shinohara H, Sawado R, Nakagawa M, Hattori A, Yamagata K, Tauchi K, et al. Dual targeting of EZH1 and EZH2 for the treatment of malignant rhabdoid tumors. Mol Ther - Oncolytics. Elsevier; 2022;27:14–25.
35. Shen X, Liu Y, Hsu Y-J, Fujiwara Y, Kim J, Mao X, et al. EZH1 Mediates Methylation on Histone H3 Lysine 27 and Complements EZH2 in Maintaining Stem Cell Identity and Executing Pluripotency. Mol Cell. 2008;32:491–502.
36. Yuan W, Xu M, Huang C, Liu N, Chen S, Zhu B. H3K36 methylation antagonizes PRC2-mediated H3K27 methylation. J Biol Chem. 2011;286:7983–9.
37. Schmitges FW, Prusty AB, Faty M, Stützer A, Lingaraju GM, Aiwazian J, et al. Histone methylation by PRC2 is inhibited by active chromatin marks. Mol Cell. 2011;42:330–41.
38. Dickson BM, Tiedemann RL, Chomiak AA, Cornett EM, Vaughan RM, Rothbart SB. A physical basis for quantitative ChIP-sequencing. J Biol Chem. 2020;295:15826–37.
39. Dickson BM, Kupai A, Vaughan RM, Rothbart SB. Streamlined quantitative analysis of histone modification abundance at nucleosome-scale resolution with siQ-ChIP version 2.0. Sci Rep. 2023;13:7508.
40. Qu X, Liang Y, McCornack C, Xing X, Schmidt H, Tomlinson C, et al. Charting the regulatory landscape of TP53 on transposable elements in cancer. Genome Res. Cold Spring Harbor Lab; 2025;35:1456–71.
41. Ferrari KJ, Scelfo A, Jammula S, Cuomo A, Barozzi I, Stützer A, et al. Polycomb-Dependent H3K27me1 and H3K27me2 Regulate Active Transcription and Enhancer Fidelity. Mol Cell. 2014;53:49–62.

42. Cui K, Zang C, Roh T-Y, Schones DE, Childs RW, Peng W, et al. Chromatin Signatures in Multipotent Human Hematopoietic Stem Cells Indicate the Fate of Bivalent Genes during Differentiation. Cell Stem Cell. 2009;4:80–93.
43. Ai S, Yu X, Li Y, Peng Y, Li C, Yue Y, et al. Divergent Requirements for EZH1 in Heart Development Versus Regeneration. Circ Res. American Heart Association; 2017;121:106–12.
44. Vo LT, Kinney MA, Liu X, Zhang Y, Barragan J, Sousa PM, et al. Regulation of embryonic haematopoietic multipotency by EZH1. Nature. 2018;553:506–10.
45. Mochizuki-Kashio M, Aoyama K, Sashida G, Oshima M, Tomioka T, Muto T, et al. Ezh2 loss in hematopoietic stem cells predisposes mice to develop heterogeneous malignancies in an Ezh1-dependent manner. Blood. 2015;126:1172–83.
46. Feng S, Zhong Z, Wang M, Jacobsen SE. Efficient and accurate determination of genome-wide DNA methylation patterns in Arabidopsis thaliana with enzymatic methyl sequencing. Epigenetics Chromatin. 2020;13:42.
47. Charlet J, Duymich CE, Lay FD, Mundbjerg K, Dalsgaard Sørensen K, Liang G, et al. Bivalent Regions of Cytosine Methylation and H3K27 Acetylation Suggest an Active Role for DNA Methylation at Enhancers. Mol Cell. 2016;62:422–31.
48. Koeppel M, van Heeringen SJ, Kramer D, Smeenk L, Janssen-Megens E, Hartmann M, et al. Crosstalk between c-Jun and TAp73alpha/beta contributes to the apoptosis-survival balance. Nucleic Acids Res. 2011;39:6069–85.
49. McLean CY, Bristor D, Hiller M, Clarke SL, Schaar BT, Lowe CB, et al. GREAT improves functional interpretation of cis-regulatory regions. Nat Biotechnol. 2010;28:495–501.
50. Lasko LM, Jakob CG, Edalji RP, Qiu W, Montgomery D, Digiammarino EL, et al. Discovery of a potent catalytic p300/CBP inhibitor that targets lineage-specific tumors. Nature. 2017;550:128–32.
51. Mousavi K, Zare H, Wang AH, Sartorelli V. Polycomb protein Ezh1 promotes RNA polymerase II elongation. Mol Cell. 2012;45:255–62.
52. Liu P, Nadeef S, Serag MF, Paytuví-Gallart A, Abadi M, Della Valle F, et al. PRC2-EZH1 contributes to circadian gene expression by orchestrating chromatin states and RNA polymerase II complex stability. EMBO J. 2024;43:6052–75.
53. Neri F, Rapelli S, Krepelova A, Incarnato D, Parlato C, Basile G, et al. Intragenic DNA methylation prevents spurious transcription initiation. Nature. 2017;543:72–7.
54. Yang X, Han H, De Carvalho DD, Lay FD, Jones PA, Liang G. Gene Body Methylation Can Alter Gene Expression and Is a Therapeutic Target in Cancer. Cancer Cell. 2014;26:577–90.
55. Lee SH, Li Y, Kim H, Eum S, Park K, Lee C-H. The role of EZH1 and EZH2 in development and cancer. BMB Rep. 2022;55:595–601.
56. Goldberg AD, Banaszynski LA, Noh K-M, Lewis PW, Elsaesser SJ, Stadler S, et al. Distinct factors control histone variant H3.3 localization at specific genomic regions. Cell. 2010;140:678–91.
57. Ran FA, Hsu PD, Wright J, Agarwala V, Scott DA, Zhang F. Genome engineering using the CRISPR-Cas9 system. Nat Protoc. 2013;8:2281–308.
58. Wiederschain D, Wee S, Chen L, Loo A, Yang G, Huang A, et al. Single-vector inducible lentiviral RNAi system for oncology target validation. Cell Cycle Georget Tex. 2009;8:498–504.
59. Wee S, Wiederschain D, Maira S-M, Loo A, Miller C, deBeaumont R, et al. PTEN-deficient cancers depend on PIK3CB. Proc Natl Acad Sci. Proceedings of the National Academy of Sciences; 2008;105:13057–62.
60. Rothbart SB, Dickson BM, Raab JR, Grzybowski AT, Krajewski K, Guo AH, et al. An Interactive Database for the Assessment of Histone Antibody Specificity. Mol Cell. 2015;59:502–11.
61. Sidoli S, Bhanu NV, Karch KR, Wang X, Garcia BA. Complete Workflow for Analysis of Histone Post-translational Modifications Using Bottom-up Mass Spectrometry: From Histone Extraction to Data Analysis. J Vis Exp JoVE. 2016;54112.
62. Joseph-Chowdhury J-SN, Stransky S, Graff S, Cutler R, Young D, Kim JS, et al. Global level quantification of histone post-translational modifications in a 3D cell culture model of hepatic tissue. J Vis Exp JoVE. 2022;10.3791/63606.

63. Yuan Z-F, Sidoli S, Marchione DM, Simithy J, Janssen KA, Szurgot MR, et al. EpiProfile 2.0: A Computational Platform for Processing Epi-Proteomics Mass Spectrometry Data. J Proteome Res. American Chemical Society; 2018;17:2533–41.
64. Cornett EM, Dickson BM, Rothbart SB. Analysis of Histone Antibody Specificity with Peptide Microarrays. J Vis Exp JoVE. 2017;55912.
65. Dickson BM, Cornett EM, Ramjan Z, Rothbart SB. ArrayNinja: An Open Source Platform for Unified Planning and Analysis of Microarray Experiments. Methods Enzymol. 2016;574:53–77.
66. Faust GG, Hall IM. SAMBLASTER: fast duplicate marking and structural variant read extraction. Bioinforma Oxf Engl. 2014;30:2503–5.
67. Ernst J, Kellis M. ChromHMM: automating chromatin-state discovery and characterization. Nat Methods. Nature Publishing Group; 2012;9:215–6.
68. Casper J, Speir ML, Raney BJ, Perez G, Nassar LR, Lee CM, et al. The UCSC Genome Browser database: 2026 update. Nucleic Acids Res. 2026;54:D1331–5.
69. Ramírez F, Dündar F, Diehl S, Grüning BA, Manke T. deepTools: a flexible platform for exploring deep-sequencing data. Nucleic Acids Res. 2014;42:W187-191.
70. Bibikova M, Le J, Barnes B, Saedinia-Melnyk S, Zhou L, Shen R, et al. Genome-wide DNA methylation profiling using Infinium® assay. Epigenomics. 2009;1:177–200.
71. Bibikova M, Barnes B, Tsan C, Ho V, Klotzle B, Le JM, et al. High density DNA methylation array with single CpG site resolution. Genomics. 2011;98:288–95.
72. Zhou W, Triche TJ, Laird PW, Shen H. SeSAMe: reducing artifactual detection of DNA methylation by Infinium BeadChips in genomic deletions. Nucleic Acids Res. 2018;46:e123.
73. Subramanian A, Tamayo P, Mootha VK, Mukherjee S, Ebert BL, Gillette MA, et al. Gene set enrichment analysis: a knowledge-based approach for interpreting genome-wide expression profiles. Proc Natl Acad Sci U S A. 2005;102:15545–50.
74. Qu X, Liang Y, McCornack C, Xing X, Schmidt H, Tomlinson C, et al. Charting the regulatory landscape of TP53 on transposable elements in cancer. Genome Res. Cold Spring Harbor Lab; 2025;35:1456–71.
75. Heinz S, Benner C, Spann N, Bertolino E, Lin YC, Laslo P, et al. Simple combinations of lineage-determining transcription factors prime cis-regulatory elements required for macrophage and B cell identities. Mol Cell. 2010;38:576–89.
76. Muzny DM, Bainbridge MN, Chang K, Dinh HH, Drummond JA, Fowler G, et al. Comprehensive molecular characterization of human colon and rectal cancer. Nature. Nature Publishing Group; 2012;487:330–7.
77. Lachmann A, Xie Z, Ma'ayan A. blitzGSEA: efficient computation of gene set enrichment analysis through gamma distribution approximation. Bioinforma Oxf Engl. 2022;38:2356–7.
78. Dyer PN, Edayathumangalam RS, White CL, Bao Y, Chakravarthy S, Muthurajan UM, et al. Reconstitution of nucleosome core particles from recombinant histones and DNA. Methods Enzymol. 2004;375:23–44.

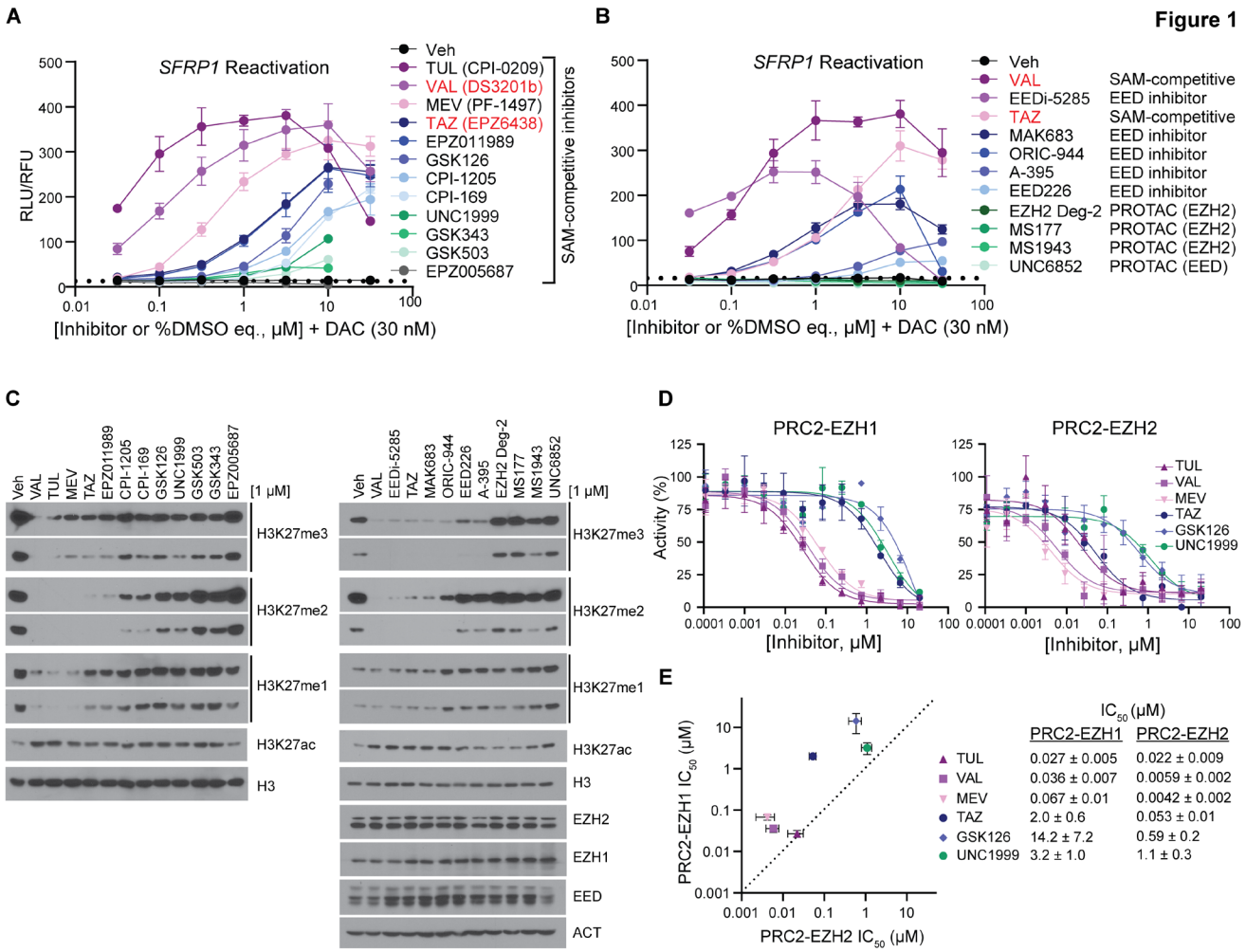

Figure 1. Dual EZH1/2 inhibition distinguishes PRC2 antagonists that potentiate DNMTi-induced transcription.

A-B) NLuc reporter activity from the endogenous *SFRP1*-NLuc locus in HCT116 DNMT1 hypomorphic cells following 72-hour treatment with the indicated PRC2 antagonists titrated with a fixed concentration of DAC (30 nM). Red text indicates SAM-competitive inhibitors shared between experiments. Relative luminescence units (RLU) are normalized to relative fluorescence units (RFU) from multiplexed CellTiter-Fluor viability assays. Data are mean ± SD of technical triplicates and representative of n=3 biological replicates. Dotted black lines denote the maximal signal measured without the addition of DAC (see Figure S1A-B). TUL, tulmimetostat; VAL, valemetostat; MEV, mevrometostat; and TAZ, tazemetostat.

C) Western blot analysis of the indicated proteins and PTMs from wild-type HCT116 cells following 72-hour treatment with vehicle (DMSO, % equivalent) or the indicated PRC2 inhibitors (1 μM) ordered approximately by ability to induce *SFRP1* expression in **A-B**. Short and long exposures are shown for H3K27 methylation states.

D) *In vitro* methyltransferase activity assays using recombinant mononucleosome substrates and PRC2 core complexes (SUZ12, EED, and RbAp46/48) containing either EZH2 or EZH1 as the catalytic subunit. Selected SAM-competitive inhibitors from **A** were titrated as indicated. Normalized results are presented as percent PRC2 activity relative to no-inhibitor control, and data are the mean ± SD of technical triplicates.

E) Comparison of IC_{50} values from **D**. Dotted line, x=y.

See also Figure S1.

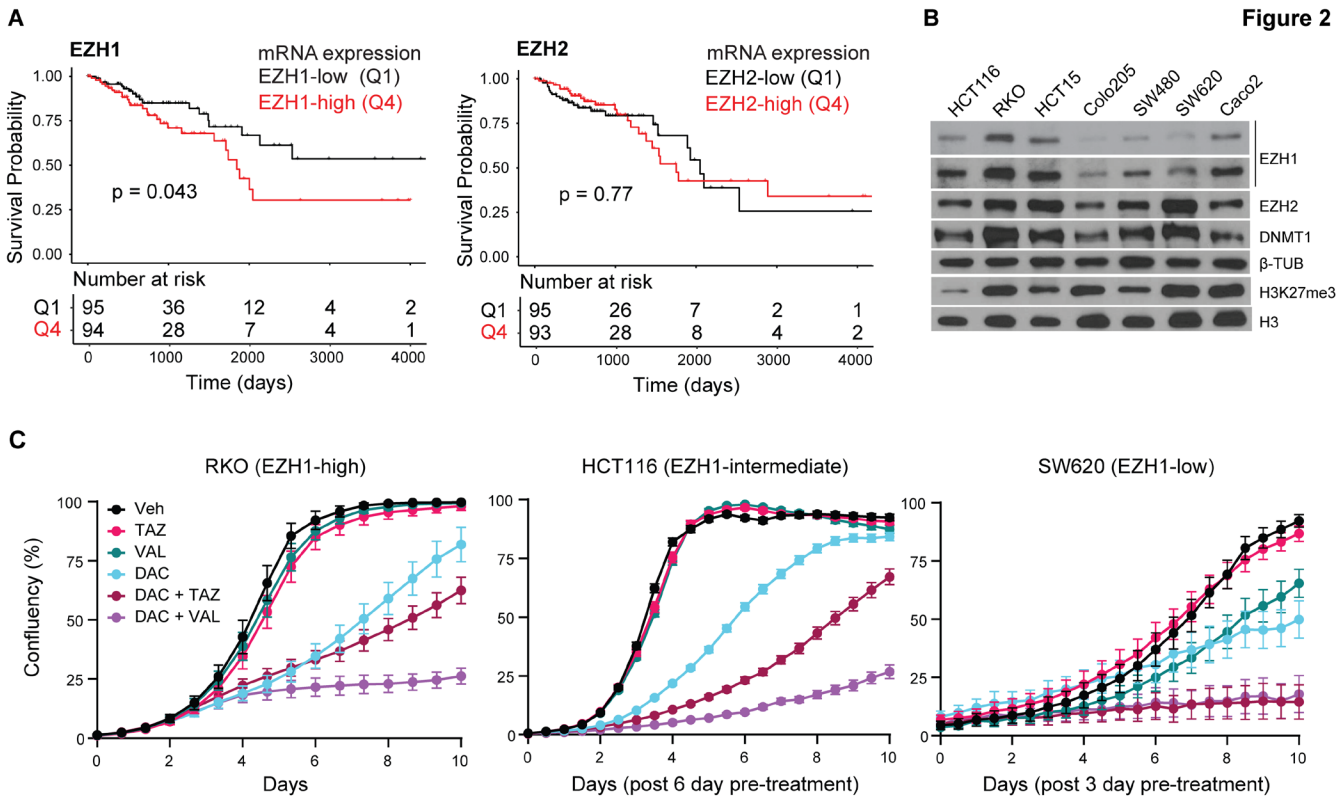

Figure 2. EZH1 expression stratifies patient survival and enhanced sensitivity to dual EZH1/2 inhibition in colorectal cancer

A) Kaplan-Meier survival curves for TCGA COADREAD patients stratified by EZH1 (left) and EZH2 (right) mRNA expression. Patients in the lowest (Q1) and highest (Q4) expression quartiles were compared to calculate significance of overall survival. n=380

B) Western blot analysis of the indicated proteins across human colon cancer cell lines.

C) Incucyte longitudinal cell proliferation measurements (% confluency) of RKO, HCT116, and SW620 cells treated with DAC (RKO and SW620, 300 nM; HCT116, 30 nM), VAL (1 μM), TAZ (1 μM), or the indicated combinations. SW620 and HCT116 were pre-treated for one or two 72-hour treatment cycles, respectively, prior to plating for growth measurements and again at Day 0. Data are the mean ± SEM of technical replicates (n=12 images per timepoint and treatment) from a single experiment and are representative of n=6 (RKO), n=3 (HCT116), and n=3 (SW620) biological replicates.

See also Figure S2.

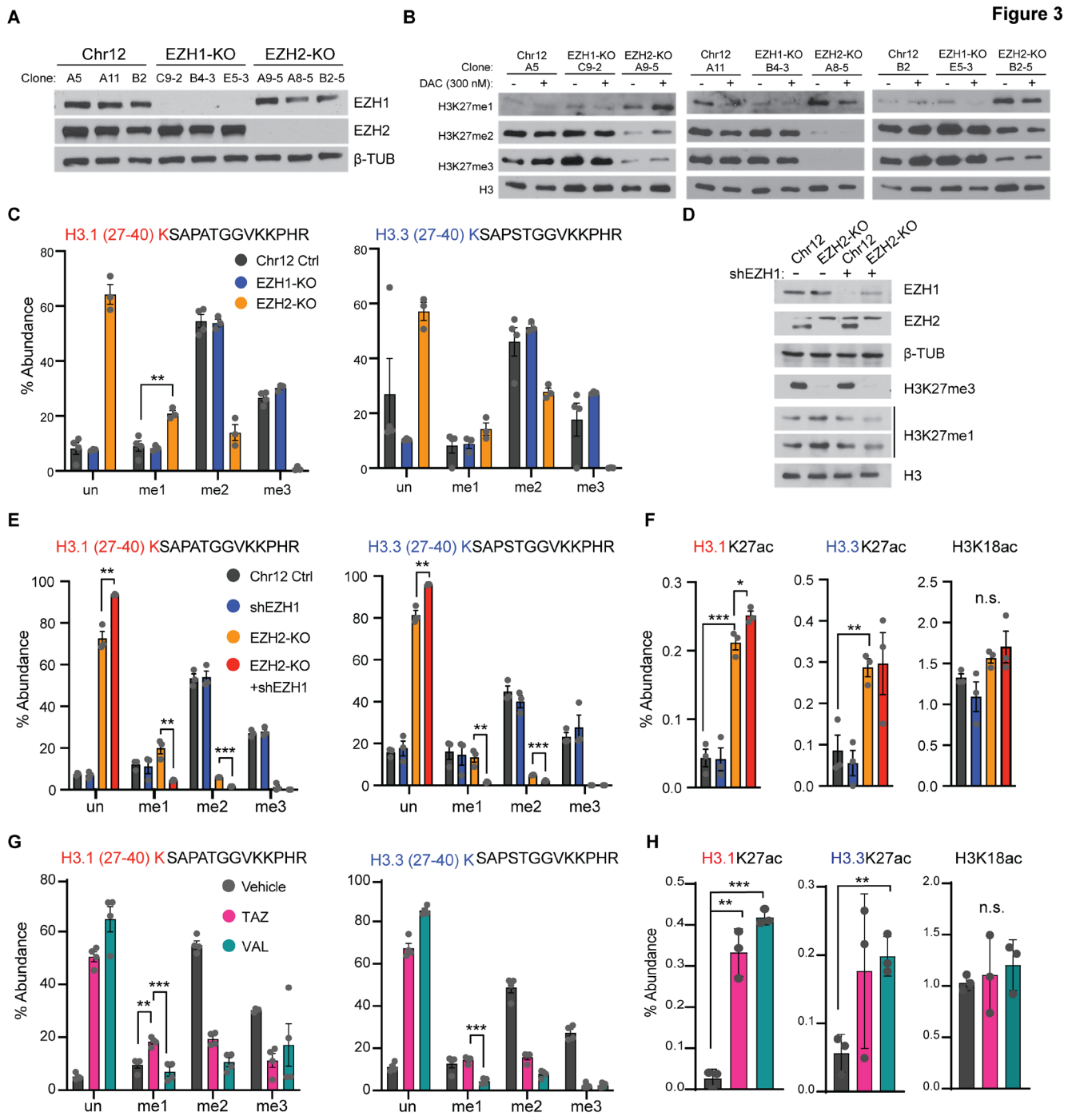

Figure 3. EZH1 maintains H3K27me1 following EZH2 genetic knockout or chemical inhibition
A) Western blot validation of EZH1 and EZH2 protein expression in RKO CRISPR/Cas9 KO clones targeting EZH1, EZH2, or a gene-desert control region on chromosome 12 (Chr12). Alphanumeric labels denote independently derived clonal populations.
B) Western blot analysis of global H3K27 methylation states in RKO CRISPR KO clones treated with vehicle or DAC (300 nM) for 72 hours.
C) Histone PTM mass spectrometry analysis of relative abundances for H3K27 methylation states on H3.1 and H3.3 in individual RKO CRISPR clones. Data are mean ± SD of three clones per genotype.
D) Western blot analysis of the indicated proteins in RKO Chr12 control (clone B2) and EZH2-KO (clone A8-5) cells following shEZH1 induction with doxycycline for 72 hours.

E-F) Histone PTM mass spectrometry analysis of relative abundances of H3K27 methylation states on H3.1 and H3.3 (**E**) or the indicated acetylated H3 peptides (**F**) in RKO Chr12 control and EZH2-KO cells following shEZH1 induction. Data are mean ± SD of n=3 biological replicates.
G-H) Histone PTM mass spectrometry analysis of relative abundances of H3K27 methylation states on H3.1 and H3.3 (**G**) or the indicated acetylated H3 peptides (**H**) in RKO cells treated with the indicated EZH inhibitors (1 μM) for 72 hours. Data are mean ± SD of n=4 biological replicates.
Red or blue "K" denotes modified lysine residues. Statistical significance was calculated using multiple unpaired t-tests. n.s., not significant; *$p<0.05$, **$p<0.01$, ***$p<0.001$.
See also Figure S3.

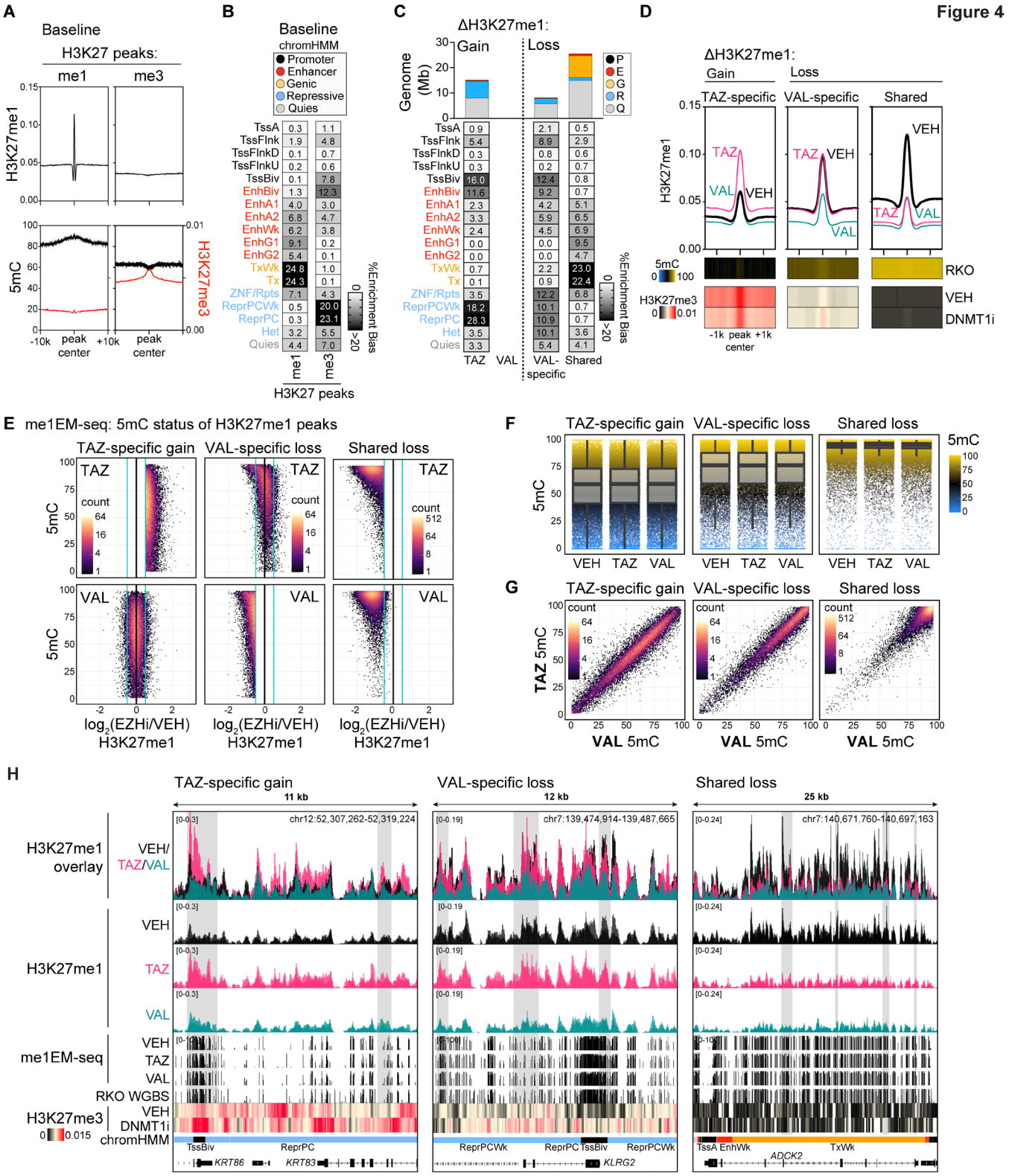

Figure 4. Genomic profiling of H3K27me1 dynamics in response to EZH inhibition.
A) Average epigenomic profiles centered on vehicle (VEH, % eq. DMSO)-associated H3K27me1 (left) or H3K27me3 (right) siQ-ChIP peaks in RKO cells. Top: H3K27me1 (siQ-ChIP); Bottom left y-axis: DNA methylation (5mC; WGBS); Bottom right y-axis: H3K27me3 (siQ-ChIP).

B) Relative enrichment bias for chromHMM states at VEH-associated H3K27me1 and H3K27me3 peaks in RKO cells.
C) chromHMM characterization of significantly altered H3K27me1 regions following 72-hour treatment with TAZ or VAL (1 μM) relative to VEH**.** Top: Genomic coverage (Mb) of H3K27me1 gains (left) and losses (right). Bottom: Relative chromHMM enrichment bias for altered H3K27me1 distributions. chromHMM legend from **B** applies.
D) Average epigenomic profiles for three classes of H3K27me1 redistribution relative to VEH-treated cells: TAZ-specific gains (left), VAL-specific losses (middle), and losses shared between TAZ and VAL (right).Top**:** H3K27me1 signal (siQ-ChIP, n=3 biological replicates per treatment); Middle: Baseline DNA methylation heatmap (WGBS, GSE262054); Bottom**:** H3K27me3 signal (previously reported RKO siQ-ChIP; GSE256135). DNMT1i=GSK3484862, 1 μM.
E) Density scatterplots from H3K27me1 siQ-ChIP coupled to enzymatic methyl sequencing (me1EM-seq) showing 5mC levels within altered H3K27me1 peaks (left: TAZ-specific gains; middle: VAL-specific losses; right: shared losses).
F) Boxplots of me1EM-seq DNA methylation distribution within altered peaks of H3K27me1 across treatment conditions.
G) Density scatterplots comparing VAL versus TAZ 5mC levels from me1EM-seq at altered H3K27me1 peaks.
H) Representative genome browser tracks illustrating baseline and treatment changes in H3K27me1, H3K27me3, and 5mC.
See also Figures S4-5.

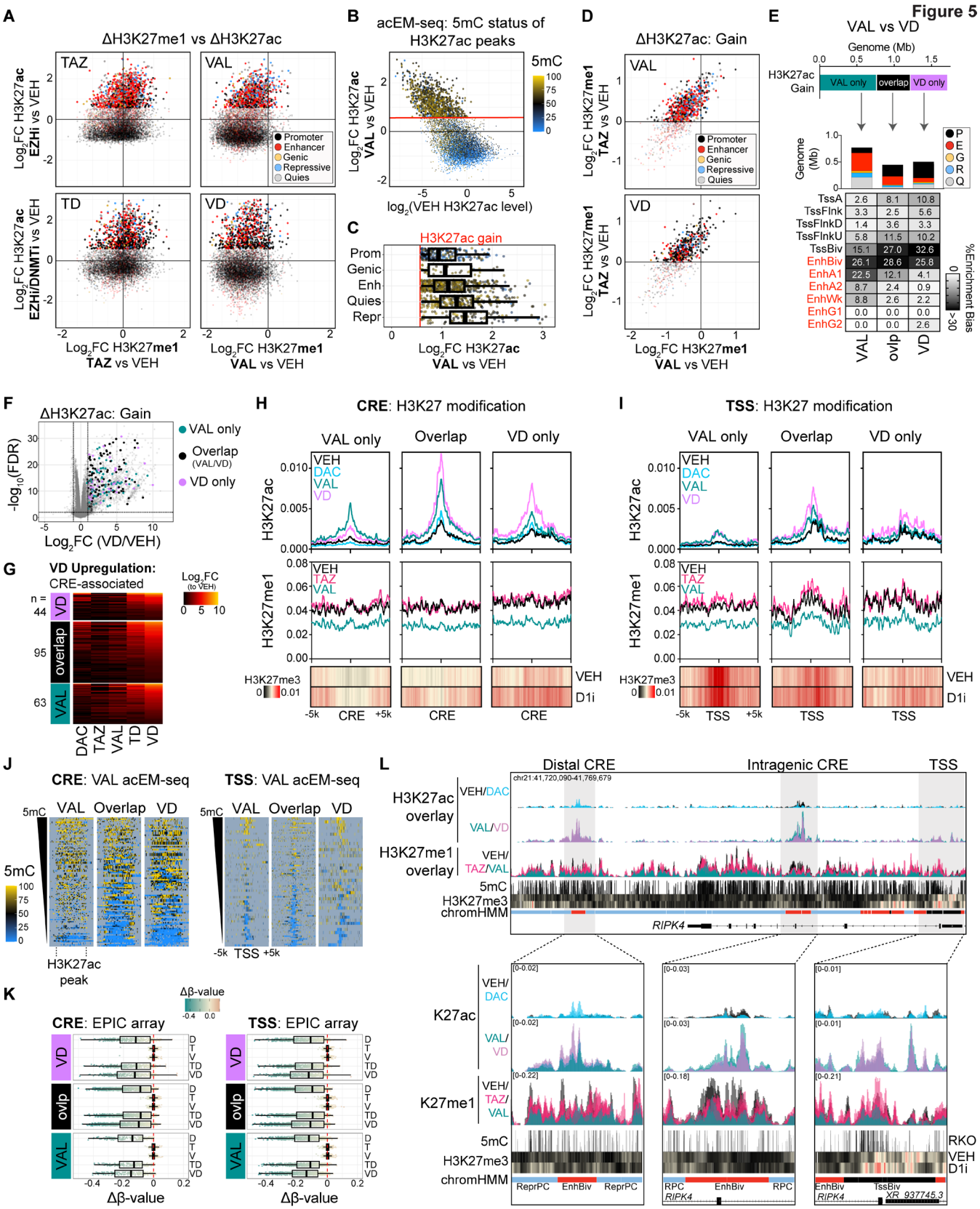

Figure 5. Genomic profiling of H3K27ac dynamics in response to EZH inhibition.
A) Scatterplots relating H3K27me1 change (x-axis) to H3K27ac change (y-axis) at loci where H3K27ac gains occur within ±10kb of H3K27me1-enriched regions. Top: EZHi monotherapy; bottom:

DNMTi/EZHi combinations. H3K27ac peaks are colored by their condensed chromHMM state. Large dots denote significant H3K27ac gains (≥ 1.5 fold; $log_2FC \geq 0.585$) relative to VEH. RKO cells were treated for 72 hours with VEH (% eq. DMSO), EZHi (TAZ or VAL, 1 uM), DNMTi (DAC, 100 nM) or combinations (TD, TAZ + DAC; VD, VAL + DAC).
B) Scatterplots relating VEH-associated H3K27ac level (x-axis) to VAL-induced H3K27ac change (y-axis) colored by average DNA methylation within each peak measured by acEM-seq in VAL-treated cells. Large dots indicate significant H3K27ac gains (≥ 1.5 fold; $log_2FC \geq 0.585$, red line) relative to VEH.
C) Boxplot of VAL-induced H3K27ac gains from **B** among chromHMM annotations. Each dot (peak) is colored by the average 5mC status derived from acEM-seq of VAL-treated samples. Legend from **B** for 5mC applies.
D) Scatterplots relating H3K27me1 changes induced by VAL (x-axis) and TAZ (y-axis) adjacent to ($\pm$10 kb) VAL-associated (top) or VD-associated (bottom) H3K27ac gains. Each dot represents a peak of H3K27ac gain, colored by chromHMM state. Large dots indicate ΔH3K27me1 $\geq$ 0 with TAZ treatment.
E) Overlap (top) and chromHMM characterization (bottom) of VAL- and VD-associated H3K27ac gains (when ΔH3K27me1 $\geq$ 0 with TAZ treatment) from **B.** Top: Stacked bar graph of H3K27ac gains in genomic coverage (Mbs). Bottom: Relative enrichment bias for altered H3K27ac gained distributions across chromHMM states.
F) Volcano plot for VD-associated gene upregulation associated with the indicated H3K27ac gains at cis-regulatory elements (CREs) from **E**.
G) Heatmap of gene expression changes (log_2FC, n=3 biological replicates per treatment) across the indicated treatments for genes described in **F**.
H - I) Average epigenomic profiles of H3K27 modifications at CREs **(H)** and TSSs **(I)** associated with upregulated genes described in **F**. Top: H3K27ac signal (siQ-ChIP efficiency, n=2 biological replicates per treatment); Middle: H3K27me1 signal (siQ-ChIP efficiency, n=3 biological replicates per treatment); Bottom: Heatmaps for H3K27me3 signal (siQ-ChIP efficiency, n=2 biological replicates) from previously reported RKO siQ-ChIP with DNMT1i treatment (GSE256135; GSK3484862, 1 μM).
J) Heatmap of 5mC levels (from acEM-seq) for H3K27ac gains at CREs and TSSs described in **H-I,** respectively. Each row represents a peak, sorted by highest to lowest 5mC levels.
K) Boxplots for change in 5mC (EPIC arrays, n=2 biological replicates per treatment), $\Delta\beta$-value relative to VEH across all single-agent and combination treatments for H3K27ac peaks described in **H-J**.
L) Representative genome browser view across the *RIPK4* locus illustrating epigenetic patterns described in **H-J**.
See also Figures S6.

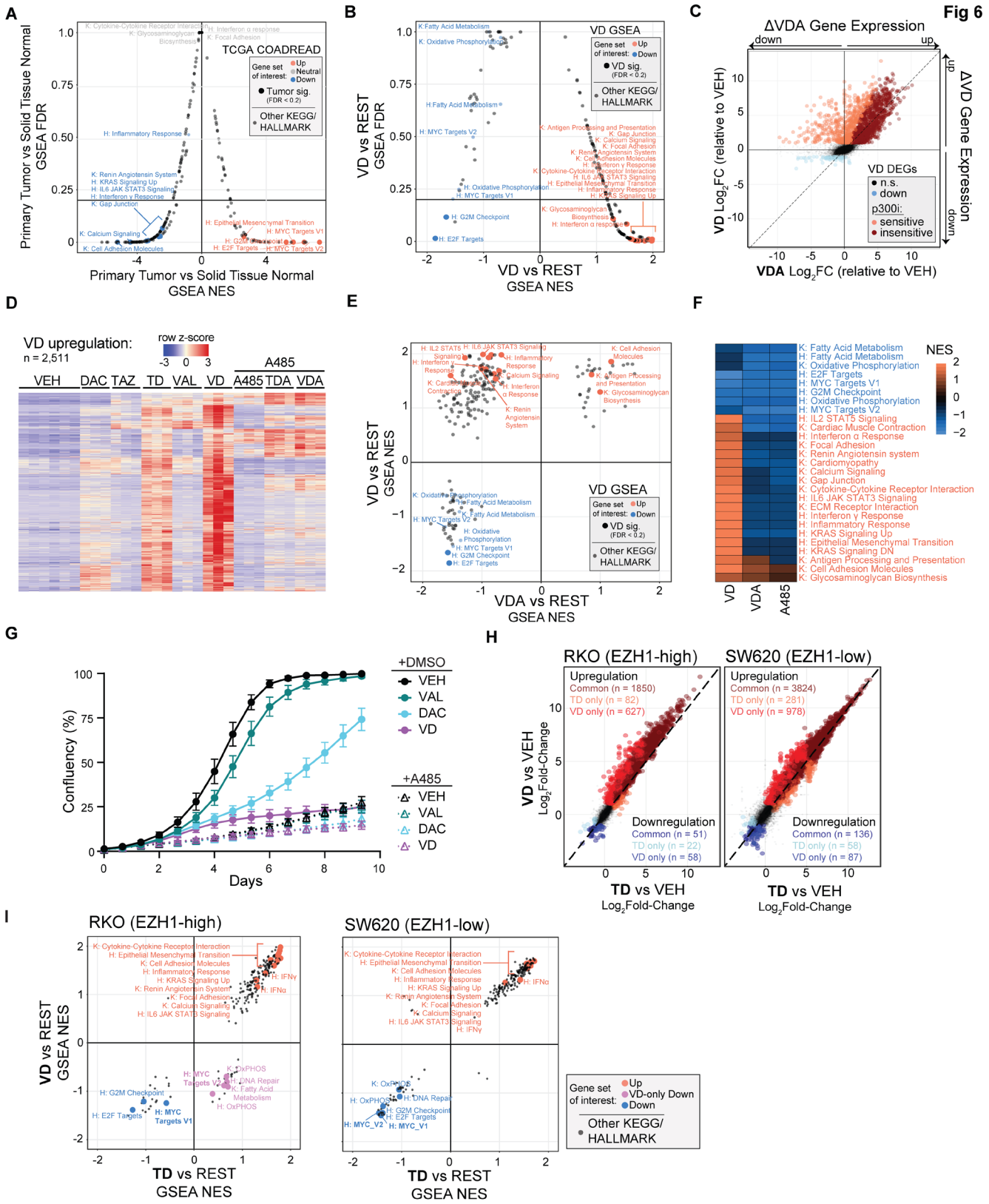

Figure 6. Combined EZH1/2i and DNMTi suppresses p300/CBP-driven oncogenic transcriptional programs

A) GSEA comparing TCGA COADREAD tumors (n=380) to normal tissue across HALLMARK (H) and KEGG (K) gene sets. NES, normalized enrichment score.

B) GSEA of VD-associated transcriptional changes compared to monotherapy treatments (REST, VEH/DAC/VAL) across HALLMARK (H) and KEGG (K) gene sets.
C) Scatterplot of gene expression change (relative to VEH) between VD treatment (y-axis) and VD in combination with the p300/CBP inhibitor A485 (A, 10 μM) (x-axis). Each dot indicates an individual gene with coordinates derived from the indicated drug treatment gene expression fold change (log_2FC) relative to VEH.
D) Supervised clustered heatmap of gene expression fold change (log_2FC) relative to VEH across drug treatments (row z-score, each row is a gene) for genes significantly upregulated by VD treatment. Approximately 83% of genes are sensitive to A485 treatment.
E) Scatterplot of GSEA results relating VD treatment (y-axis) to VDA treatment (x-axis) compared to all other monotherapy and combination treatments (REST). Each dot indicates an individual gene set NES for the indicated drug treatments within the HALLMARK/KEGG gene sets.
F) Supervised clustered heatmap of NES across drug treatments for gene sets of interest from **E**.
G) Incucyte longitudinal cell proliferation measurements (% confluency) of RKO cells treated with DAC (300 nM), VAL (1 μM), or the combination with or without A485 (10 μM). Data are the mean ± SEM of technical replicates (n=12 images per timepoint and treatment) from a single experiment and are representative of n=3 biological replicates.
H) Scatterplot relating gene expression change (log_2FC relative to VEH) for TD (TAZ+DAC) treatment (x-axis) and VD treatment (y-axis) in RKO and SW620 cells. Differentially expressed genes are highlighted by color and distinguished by shade as Common, TD only, or VD only genes.
I) Comparative GSEA analysis (NES) for KEGG and HALLMARK gene sets between TD (x-axis) and VD (y-axis) compared to all other treatments in RKO and SW620 cells.
See also Figure S7.

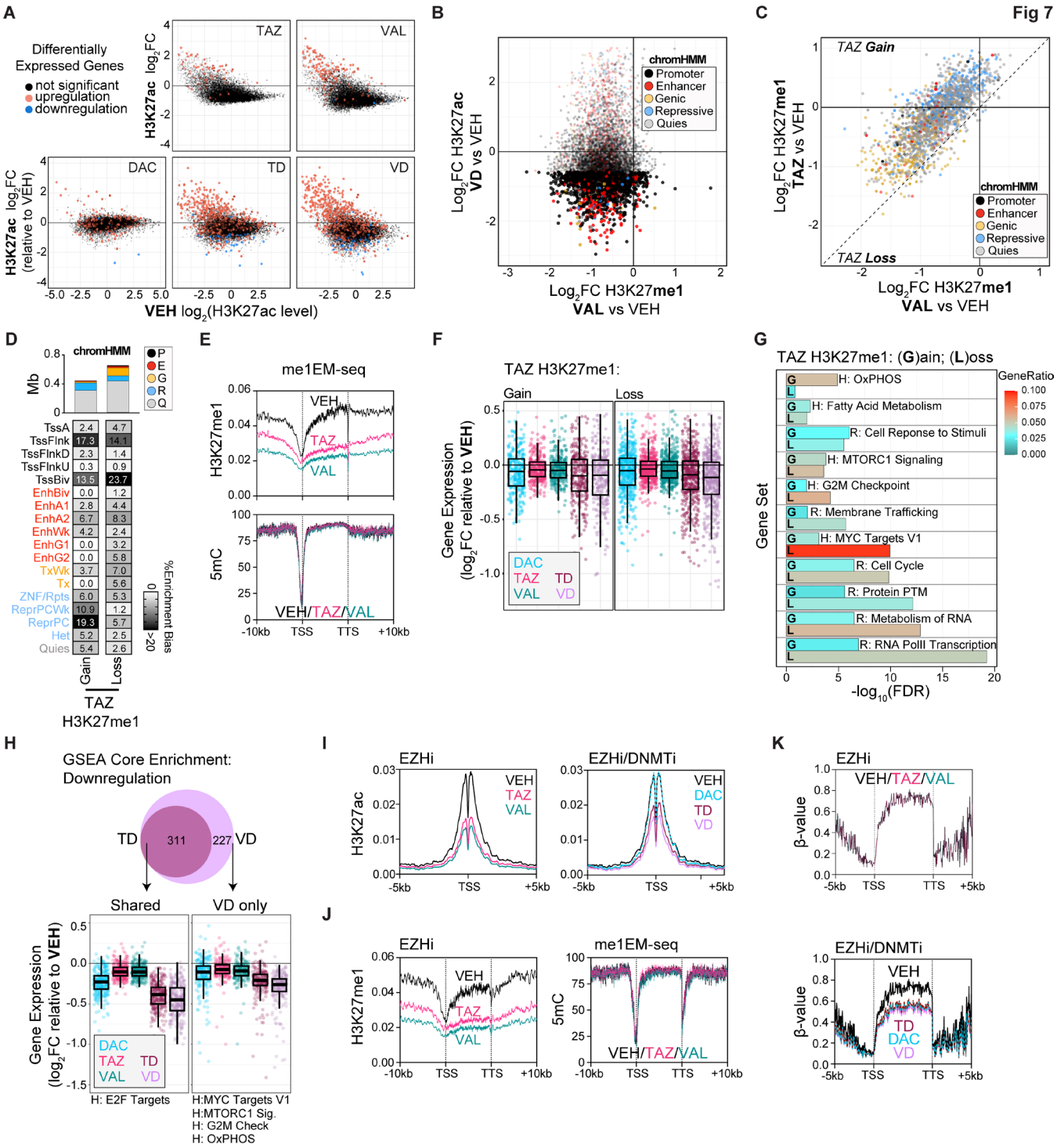

Figure 7. Cooperative repression of oncogenic transcription programs by DNMTi/EZHi coincides with coordinated loss of active chromatin features.

A) MA plots relating baseline H3K27ac levels in VEH (x-axis) to change in H3K27ac level for the indicated drug treatments relative to VEH (y-axis). Each dot indicates H3K27ac peaks ±10kb of a gene promoter. Differentially expressed genes for each drug treatment are highlighted with their associated H3K27ac peak.

B) Scatterplot relating VAL-associated H3K27me1 change (x-axis) to VD-associated H3K27ac change (y-axis) that occurred ±10kb of H3K27me1 signal. H3K27ac peaks are colored by their chromHMM state. Large dots indicate significant H3K27ac loss (FC ≤ -1.5, $\log_2$FC ≤ -0.585) relative to VEH.

C) Scatterplot relating VAL-associated H3K27me1 change (x-axis) to TAZ-associated H3K27me1 change (y-axis) at H3K27me1 ±10kb to regions of H3K27ac loss described in **B**. H3K27me1 peaks are colored by their chromHMM state.
D) chromHMM characterization for nearest H3K27me1 peaks (±10kb) to regions of H3K27ac loss shown in **C.** Top: Genomic coverage (Mbs) of TAZ-specific H3K27me1 gains (left) and losses (right). Bottom: Relative enrichment bias for H3K27me1 peaks described in **C**. chromHMM legend from **C** applies.
E) Average H3K27me1 (top) and 5mC (bottom) (me1EM-seq, n=2 biological replicates) signal across gene bodies for the genes underlying the epigenetic signatures described in **C**.
F) Boxplots for gene expression change across drug treatments (log_2FC relative to VEH, n=3 biological replicates per treatment) for genes associated with H3K27ac loss (from **B**), with either TAZ-specific H3K27me1 gains (left) or losses (right) ±10kb to the gene promoter. Each dot indicates an individual gene.
G) Enrichment for HALLMARK (H) and REACTOME (R) gene sets using genes shown in **E**, separated by TAZ-specific H3K27me1 gain (G) or loss (L).
H) Gene expression change for overlapping (shared) and unique (VD only) core enrichment genes from TD- and VD-associated GSEA downregulated gene sets (from **Figure 6I**). Each dot represents an individual gene. Enriched gene sets listed below box plot.
I) Average H3K27ac profiles (siQ-ChIP efficiency, n=2 biological replicates) for all VD-associated GSEA downregulated core enrichment genes (from **H**, n=538), centered on the TSS.
J) Average H3K27me1 (left) and 5mC (right) (me1EM-seq, n=2 biological replicates) signal across gene bodies for all VD-associated GSEA downregulated core enrichment genes (from **H**, n=538).
K) Average 5mC profiles (EPIC array, n=2 biological replicates) across gene bodies of all VD-associated GSEA downregulated core enrichment genes (from **H**, n=538).
See also Figure S8.